GROUTED SLEEVE CONNECTIONS USED IN PRECAST REINFORCED CONCRETE CONSTRUCTION - EXPERIMENTAL INVESTIGATION OF A COLUMN-TO-COLUMN JOINT

Nerio TULLINI[a], Fabio MINGHINI[b]

Engineering Department, University of Ferrara, Via Saragat 1, Ferrara, Italy

[a] Corresponding author. E-mail: nerio.tullini@unife.it

[b] E-mail: fabio.minghini@unife.it

ABSTRACT

The results of an experimental campaign concerning full-scale tests on precast reinforced concrete column-to-column connections made with grouted sleeve splices are presented. The precast column units had a square cross-section with the side of 500 mm. Eight 20 mm-diameter bars protruding from one unit were grouted into corrugated steel sleeves encased in the other unit. The column-to-column connections were subjected to four monotonic tests (axial tension, bending with and without axial compression, and shear) and to one cyclic bending test.

In the tension test failure took place far from the interface between the precast units and highlighted the effectiveness of the stress transfer along the splice region. In all other tests, damage developed at the interface between the two units. In the bending tests with and without axial compression significant over-strengths with respect to design resistances computed for equally-reinforced monolithic members were attained. Because of the reduced thickness of the interface between the precast units, the rotation that concentrated at the interface led to a moderate reduction of the global bending stiffness. In the shear test the pure shear capacity of the bars crossing the joint was achieved. The cyclic bending test showed a ductile and stable hysteretic behavior of the connection.

Keywords: Precast concrete columns; Column-to-column connection; Grouted sleeve connection; Static tests; Cyclic tests

1. INTRODUCTION

The structural behavior of precast Reinforced Concrete (RC) frames is essentially ruled by the connections between the various monolithic elements. Therefore, an appropriate connection design is a major key to a successful prefabrication. Connection performance is influenced by multiple factors, including building manufacture, erection and maintenance. The great interest for the role of the connections between precast elements is shown by numerous publications available on this topic [1−8].

Precast industrial buildings not based on seismic design criteria may suffer heavy damages even in the presence of moderate earthquakes. Just to keep to a recent example, in the case of the 2012 Emilia earthquakes [9], absence or inadequacy of connecting systems between the precast members determined disastrous losses of support of roof slabs or main girders in a huge number of buildings [10]. For this reason, modern seismic design codes require adequate structural ductility and compliance with capacity design. To this aim, the seismic performance of precast concrete structures was extensively investigated over the last decade within several European research projects [11−13], and design rules for connections in precast structures were published in a specific booklet [14].

In Japan' and New Zealand's extensive experience, several monolithic equivalent, ductile precast RC construction systems incorporating non-prestressed connections were developed for a weak beam-strong column behavior [4, 6, 15−17].

In the connection system referred to as System 2 in [4, 15], suitable for multi-story buildings, the protruding longitudinal bars from the column below cross vertical holes preformed in the precast beam unit and extend above the top surface of the beam itself (see for example Fig. 5-9 in [6] or Fig. 11 in [15]). The columns of the story above, provided with steel sleeves in the bottom part, are positioned above the top surface of the beam units, so as to receive the longitudinal bars of

the lower columns. The sleeves in the columns are then grouted to obtain full continuity at the connections.

In the system referred to as System 3 in [4, 15], T-shaped precast units are connected with one another using grouted steel sleeves for the column bars and cast-in-place joints at midspan for the beams (see for example Fig. 5-13 in [6] or Fig. 4c in [15]). Therefore, also this system requires the continuity of the column reinforcement through a grouted joint, typically located at the column bottom end.

Recently, a very ductile connection technology suitable for precast frames to be realized in high-seismicity regions was proposed in [18].

With particular regard to the connections between precast column elements, or between precast columns and their foundations, two main approaches may be used.

The first approach ensures the continuity of the column longitudinal reinforcement making use of proprietary grouted steel sleeves [6, 19]. A general detail of the connection system is shown in Fig. 5-33 reported in [6] (see also Fig. 13 in [15]). The use of steel sleeves requires the oversizing of the transverse reinforcement in the proximity of the column end sections, and may determine a greater distance between longitudinal bars and concrete surfaces with respect to the cast-in-place construction.

The second approach consists in using non-contact lap splices of the longitudinal column bars [4, 6, 15–17, 20–26]. A general detail of the connection system is shown in Fig. 5-35 reported in [6]. In particular, the longitudinal bars protruding from one column unit are grouted into corrugated steel ducts encased in the other unit. Adjacent to each duct, two smaller-diameter bars are present, each having at least half of the cross-section area of every grouted bar.

When used for column-to-foundation joints in seismic regions, the previously described connection systems represent a viable alternative to the traditional construction method involving monolithic columns inserted into a precast or cast-in-place pocket foundation.

In spite of its considerable simplicity, the connection system using non-contact lap splices of the column bars still lacks a comprehensive experimental characterization. In [20] and [21], the results of tests in the presence of bending and axial compression were presented. The grouted sleeve connections showed ultimate capacities comparable to that of monolithic columns and damages restricted to the joint section. The columns presented a square cross-section with the side of 200 mm, where four corrugated steel tubes with the diameter of 50 mm were arranged. Therefore, the dimensions of the test specimens barely were of practical use.

Similar connection systems, but specifically tailored to column-to-foundation joints, were proposed and tested in [23–25] and, recently, in [26].

In [25], the cyclic response of grouted sleeve connections (labeled "GS4") was compared with those of a cast-in-place column-to-foundation connection ("CP") and of a precast column inserted into a pocket foundation ("PF"). All columns had square cross-section with the side of 400 mm. In specimens "GS4", the connection was obtained by means of four 26 mm-diameter projecting bars protruding from the foundation and grouted into the sleeves encased in the column. Adjacent to each sleeve, two 18 mm-diameter longitudinal bars were positioned. Thus, the reinforcement ratio of the joint section was substantially coincident with that of the precast column. Specimens "GS4" showed localization of flexural cracks at the column base. Their moment resistance was almost the same as that of the other specimens. Due to the confinement induced by the steel sleeves on the grout, that prevented buckling of the projecting bars, a higher displacement capacity was obtained in comparison with specimens "CP" and "PF". To obtain a further reduction of the column damage, and then make the post-seismic repair easier, the adoption of an unbonded length of the grouted bars was also proposed in [25, 27].

In the column-to-foundation connection system recently described in [28], the bars protruding from the bottom column section are inserted into box-section steel tubes embedded in the footing, and then grouted. The square column cross-section has the side of 400 mm. A 133 mm-diameter steel centring tube is used to facilitate the assembly phase. This tube extends into the column for

380 mm, yielding a contribution to stiffness and strength of the connection, and moving the critical region upwards.

Also in bridge structures the joints between precast concrete components play an important role on the overall seismic performance. Recently, prefabricated bridge elements and systems were reviewed in [29], where grouted duct connections for column-to-footing and column-to-cap beam joints were presented.

In the present paper, a grouted sleeve connection for precast RC columns that makes use of non-contact lap splices of the longitudinal bars is proposed (Fig. 1). A detailed description of the connection system is reported in Section 2. Differently from the experiments available in the literature on similar connections, generally restricted to the case of cyclic bending in the presence of a constant axial compression [20–26], the experimental campaign presented in this and in a subsequent research was aimed at a comprehensive characterization of the connection proposed.

In this paper, four combinations of axial load N and bending moment M were investigated, i.e., (1) axial tension ($N \neq 0$, $M = 0$), (2) monotonic and (3) cyclic bending ($N = 0$, $M \neq 0$), and (4) combined axial compression and bending ($N \neq 0$, $M \neq 0$). In addition, a test with the joint section subjected to a prevailing transverse shear was conducted. Note that the connection is referred to as column-to-column connection, although a compressive axial load was applied to the specimen in only one of the tests. In fact, columns in single-story buildings or peripheral columns in multi-story buildings may be subjected to a very low axial compression.

In a subsequent research, the same connection system will be tested in cyclic bending combined with constant axial compression.

2. DESCRIPTION OF THE GROUTED SLEEVE CONNECTION

The connection is obtained by lap-splicing the longitudinal reinforcing bars of two stub columns (Fig. 1a). The column units have square cross-section with the side of 500 mm. Stub column A contains eight corrugated steel sleeves. Just as many projecting bars are encased in stub column B.

To realize the connection, stub column A is lowered into the right position, so as to insert the bars protruding from stub column B into the corrugated sleeves. The sleeves are then grouted using high-strength shrinkage-compensated mortar. The interface gap of 10 mm between the column units is sealed at the same time.

The total length of the lap splice is 2 m (Fig. 1b). The regular longitudinal reinforcement of the column units is comprised of 20 mm-diameter deformed bars placed at mid-sides and corners of the cross-section (cross-section D-D in Fig. 1c). The projecting reinforcement is also comprised of 20 mm-diameter deformed bars encased in stub column B (cross-section A-A in Fig. 1c). The corrugated sleeves encased in stub column A (cross-section C-C in Fig. 1c) present outer diameter of 63 mm and thickness of 0.8 mm. The joint section is characterized by the presence of the eight projecting bars only (cross-section B-B in Fig. 1c), resulting in a reinforcement ratio $\rho_l = 0.01$. Along the lap splice, square and diamond-shaped stirrups with the diameter of 8 mm and spacing of 100 mm are provided (Fig. 2). The clear concrete cover is 42 mm. Therefore, the minimum distance of the centroidal axis of regular and projecting bars to the concrete surfaces is 60 and 80 mm, respectively (Fig. 1c). The aforementioned reinforcement details comply with the recommendations reported in Section 8 of [30]. Note that, in analogy with precast structural typologies common in Italy, the column units are provided with a 100 mm-diameter drainpipe in centroidal position.

In Fig. 3 the cross-section located along the splice region of stub column A is compared with the column cross-section of the connection system investigated in [26], similar to that analyzed in [25]. In the present proposal the corrugated sleeves are positioned along the sides of the column cross-section rather than at the corners. This arrangement allows for the use of traditional reinforcement cages for the stub columns, presenting steel bars at both mid-side and corners of the cross-section.

All test specimens used for the experiments presented hereinafter were prepared according with the details shown in Figs. 1 and 2. The assembly phase of one of these specimens is shown in Fig. 4. The two holes in the front side of the upper column unit in Fig. 4a correspond to steel sleeves to

be grouted. Fig. 4b highlights the insertion of the projecting bars of the lower stub column into the steel sleeves of the upper stub column.

3. MATERIAL PROPERTIES

3.1. Concrete

During each of the days scheduled for casting the stub columns used to assemble the various test specimens, 150mm cubes were moulded to be tested in compression. Four cubes were tested for each specimen. Each group of four cubes was tested just before the test on the corresponding precast specimen, so ensuring the same concrete age t. The mean values $f_{cm,cube}(t)$ of the cubic compressive strengths and the corresponding values $f_{cm,cube}(28) = f_{cm,cube}(t)/\beta_{cc}(t)$ at $t = 28$ days are reported in Table 1, where coefficient $\beta_{cc}(t)$ is computed in accordance with [30]. These strengths allow for referring, in design calculations, to strength class C50/60 (characteristic strength $f_{ck} = 50$ MPa), which is the minimum of the classes reported in [30] that are compatible with the measured strengths.

Also reported in Table 1 are the mean cubic compressive strengths of the grout used for connecting the precast column units. In particular, the grout referred to as Grout 1 was adopted for the specimens tested in tension and bending, whereas that referred to as Grout 2 was used for the specimen subjected to combined bending and axial compression, and for that tested in shear. Two 150mm cubes were tested for each type of grout.

3.2. Reinforcing steel

The mean values of the experimentally determined properties for 20 mm- and 8 mm-diameter bars are reported in Table 2. Three steel specimens were tested for each diameter.

4. TESTS ON THE COLUMN-TO-COLUMN CONNECTION

In this Section, the results obtained from five tests on the column-to-column connection are reported.

All tests were load controlled with the exception of the cyclic bending test (see Section 4.3), where a displacement control was adopted for the last eight cycles. The loads were applied statically using hydraulic jacks with nominal capacity of 1 MN. The pressure in the oleodynamic circuit activating the jacks was measured using pressure transducers with nominal capacity of 700 bar. For each jack the applied load was obtained by the product of the pressure times the cylinder effective area declared by the manufacturer. Linear displacement transducers with stroke length of 150 or 200 mm were used to measure strains and displacements. All transducers were connected to a data acquisition system and powered by a stable 10 V power supply. A LabVIEW code [31] was developed for a real-time control of strains and deflections.

With regard to the strain measurements, indicating with u_i the displacement measured by the i-th displacement transducer, Li, and with b_i the initial (undeformed) distance between the two points corresponding to the connections of transducer Li to the specimen, the average strain within b_i was estimated from the following relation:

$$\varepsilon_i = u_i/b_i \tag{1}$$

4.1. Direct tension test

The test was aimed at verifying the effectiveness of the tensile stress transfer mechanism in the lap zones.

4.1.1. Specimen layout and testing protocol

The plan view of the experimental setup, showing the reinforcement layout, is reported in Fig. 5a. Both precast units were provided with a RC block of dimensions 1.5×1.0×0.5 m at the opposite sides with respect to the joint section, resulting in two corbels that allowed for the application of the

tensile load (see Paragraph 4.1.2). The specimen was placed horizontally on the pavement of the laboratory. To allow for a free specimen elongation, some 50 mm-diameter steel rolls were put between the pavement and the bottom surface of the specimen.

A preliminary loading cycle between 0 and 150 kN was carried out to check the setup of instruments and data acquisition system, with the latter load being chosen as about 10% of the expected ultimate load (evaluated as $A_{sj}f_{tm}$, with f_{tm} and A_{sj} reported in Tables 2 and A.1, respectively). Then, the tensile load was increased monotonically until failure.

4.1.2. Testing equipment and measuring system

The tensile load was applied by means of two equal jacks installed on the corbels of precast unit A and acting on two precast columns with cross-section dimensions 0.3×0.5 m connected through a 20 mm-diameter dowel to the corbels of unit B.

To measure the jack forces, for redundancy, two 1 MN-full scale load cells with nominal sensitivity 2 mV/V (labeled LC1 and LC2 in Fig. 5b) were used in addition to the pressure transducers.

Eleven displacement transducers (labeled L1 to L11 in Fig. 5b) were used to measure the horizontal displacements. Three different values of b_i were adopted for the strain evaluation: b_i = 160 mm for i = 1 to 5, b_i = 400 mm for i = 7 to 10, and, finally, b_i = 500 mm for i = 6 and 11. A view of the specimen at the beginning of test is shown in Fig. 6a.

4.1.3. Experimental results

The cracks concentrated at the joint section and outside the lap zones. Conversely, no significant crack pattern was observed along the lap splice. In Fig. 6b, the crack pattern observed at the end of test immediately outside the lap zone of unit A is shown. In that location the rupture of the reinforcing bars occurred. A maximum tensile load N_m = 1672 kN was attained.

The plots of the total applied load versus axial strains measured at the joint section and in the lap zone of unit A are reported, with solid lines, in Figs. 7a and 7b, respectively.

With regard to the joint section, thick and thin solid lines in Fig. 7a refer to the average strains experienced by top and bottom surfaces of the specimen, respectively, and were obtained from the following relations:

$$\varepsilon_{top} = (\varepsilon_1 + \varepsilon_3)/2, \qquad \varepsilon_{bot} = (\varepsilon_2 + \varepsilon_4)/2 \tag{2a, b}$$

with ε_i (i = 1 to 4) being the strain obtained from Eq. (1) for the transducers placed on the vertical sides of the specimen (see Fig. 5b). In Fig. 7a, the contribution due to the hardening of the projecting bars is clearly distinguishable for axial loads larger than 1430 kN in the case of ε_{top} and 1270 kN in the case of ε_{bot}. Top and bottom strains took the maximum values 6.8% and 8.2%, respectively. This difference was produced by the specimen self weight that gave rise to a certain amount of bending in the vertical plane. In fact, no supporting steel roll was placed between pavement and test specimen for a span length of 4.4 m approximately centred on the joint section. Due to the locations of steel rolls shown in the side view Fig. 5a, a statically indeterminate continuous beam is obtained. Neglecting the contributions due to the end corbels, the specimen self weight per unit length, equal to 5.9 kN/m, leads to a maximum bending moment M_w = 14 kNm in the intermediate span. The actual bending moment was lower than M_w. After cracking, this moment was resisted by the eight projecting bars crossing the joint section.

With regard to the lap zone of precast unit A, the plots reported with thick and thin solid lines in Fig. 7b refer to strains ε_9 and ε_{10} (see Fig. 5b), respectively. These strains were more than one order of magnitude lower than those measured at the joint section.

4.1.4. Analytical interpretation

The mean tensile stress in the projecting bars corresponding to the maximum load attained in the test is given by $f_{ta} = N_m/A_{sj} = 666$ MPa, where index "a" stands, here and in the following, for analytical quantity and A_{sj} is reported in Table A.1. This stress is approximately 5% larger than

mean tensile strength f_{tm} of the 20 mm-diameter bars reported in Table 2. This discrepancy may be due to the fact that the steel bars tested in tension belonged to a different batch with respect to those used in the reinforcement cage of the specimen. By assuming an increment of 1.05 also for the yield strength f_{ym} reported in Table 2, the analytical yield strength $f_{ya} = 1.05 f_{ym} = 540$ MPa is obtained. Correspondingly, the computed tensile load at yielding is $N_{ya} = f_{ya} A_{sj} = 1356$ kN.

Dashed lines in Fig. 7a refer to the estimates of tensile strains at the joint section, evaluated under the plane section assumption. In the linear elastic range, these estimates were obtained from the following relations:

$$\varepsilon_{top,a} = N/(E_s A_s) - M_w(H/2 - y_1)/(E_s I_s) \quad (3)$$

$$\varepsilon_{bot,a} = N/(E_s A_s) + M_w(H/2 - y_1)/(E_s I_s) \quad (4)$$

where $y_1 = 80$ mm is the distance of the centroidal axis of the projecting bars to the concrete surfaces (see cross-section B-B in Fig. 1c). Moreover, $E_s A_s$ and $E_s I_s$ represent axial and bending rigidities, respectively, evaluated for a cross-section comprised of the eight 20 mm-diameter projecting bars only, and the corresponding values are reported in Table A.2.

By imposing the yielding of the bottom bars, i.e. $\varepsilon_{bot,a} = \varepsilon_{ya} = f_{ya}/E_s$ in Eq. (4), the corresponding axial load becomes

$$N_{ya,bot} = (E_s A_s)\,[\varepsilon_{ya} - M_w(H/2 - y_1)/(E_s I_s)] = N_{ya} - M_w A_s (H/2 - y_1)/I_s = 1234 \text{ kN} \quad (5)$$

related to the first change in slope of the thin dashed curve in Fig. 7a. For axial load greater than $N_{ya,bot}$, linear-hardening elastic-plastic behavior of the steel bars has to be considered, with yield and ultimate strengths equal to f_{ya} and f_{ta}, respectively. In this case, an iterative procedure is required, where each pair (N_a, M_a) of stress resultants is computed for a trial value of the curvature and is updated until convergence is achieved as $|M_a - M_w| \le \text{tol}$, being $\text{tol} = 0.001$ kNm a prescribed tolerance. For instance, the axial load at yielding for the bars at $y_1 = 80$ mm from the top surface is equal to 1461 kN, corresponding to the change in slope of the thick dashed curve in Fig. 7a.

The discrepancy between measured and estimated axial strains highlighted in Fig. 7a, approximately equal to 0.73% in correspondence of the bar yielding, may be caused by the slip of the grouted bars with respect to the surrounding concrete.

The linear elastic load-strain responses shown in Fig. 7b refer to a generic cross-section located in the lap zone and present stiffnesses K_I (uncracked concrete) and K_{II} (cracked concrete) reported in Table A.2. As expected, the measured responses coincide with that of an uncracked concrete section up to cracking. Once the first cracking load is exceeded, the experimental response gradually tends to approach the dashed line with slope K_{II}. Analogous results were obtained for the lap zone of unit B. Therefore, with the exception of a very narrow region in proximity of the joint section, the proposed connection ensures a tension behavior analogous to that of traditional RC members.

4.2. Four-point bending test

This and next tests, where the specimen is subjected to bending without axial load, can be regarded as representative for the case of columns subjected to a very low axial compression, as is typical of peripheral columns supporting a light roof in industrial building.

4.2.1. Specimen layout and testing protocol

The specimen, constituted by two 2.1 m-long precast units, was installed into a reaction frame and simply supported in proximity of the end sections (Fig. 8a). The span length was 4 m, with the joint section being located at midspan. A symmetrical four-point bending test configuration was adopted, with each of the vertical loads being applied at a distance a = 1.4 m from the nearest support.

Three preliminary loading cycles, with the total applied load ranging between 0 and 100 kN for the first two cycles and between 0 and 150 kN for the third one, were carried out. The first two cycles were simply used to check the setup of instruments and data acquisition system and did not cause any damage to the specimen. The third cycle was intended to slightly exceed the first

cracking load capacity of a traditional RC beam with equal dimensions and reinforcement layout as the joint section. Then, the load was increased monotonically until failure.

4.2.2. Testing equipment and measuring system

The loads were applied using the same jacks as for the tension test and measured making use of pressure transducers. Ten linear displacement transducers were used to measure average strains and deflections (Fig. 8b). Transducers L1 to L6, with b_i = 100 mm (i = 1 to 6), were used to measure the strains in the longitudinal direction. Transducers L7 and L8 were used to measure the midspan deflection. Transducers L9 and L10, placed at the end supports, were used to capture possible rigid body displacements of the test specimen due to deformations of the reaction frame. A detail view of the specimen before the test is reported in Fig. 9a.

4.2.3. Experimental results

The damage mainly affected the joint section (see Fig. 9b), where the bottom reinforcing bars yielded, and then broke after an average tensile strain $\varepsilon_1 = 7.70\%$ was attained. Note that ε_1 was obtained from the measurements of transducer L1, positioned at the same distance from the specimen bottom surface as the bottom projecting bars (Fig. 8b). The average maximum compression strain calculated based on L5 measurements was $\varepsilon_5 = 0.74\%$. The maximum applied load per jack attained in the test was P_m = 251 kN, resulting in a maximum bending moment $M_\mathrm{m} = P_\mathrm{m}a$ = 352 kNm.

The plot of the applied load per jack versus net vertical deflection u_m at midspan is reported with solid line in Fig. 10. Deflection u_m was computed by subtracting the mean value of the displacements measured at the end supports from the displacement recorded by transducer L7. The correspondence between applied load P and bending moment values $M = Pa$ is also provided in Fig. 10. The sudden resistance drop for u_m = 37 mm is related with the rupture of the bottom projecting bars at the joint section.

The experimentally determined moment-average curvature relationships for a cross-section of stub column B located in the constant moment region in proximity of the joint section (χ_{stB}) and for the joint section itself (χ_{joint}) are reported in Fig. 11a (solid lines). Average curvatures χ_{joint} and χ_{stB} were obtained from the following relations:

$$\chi_{joint} = (\varepsilon_2 + |\varepsilon_5|)/d_\chi \quad (6)$$

$$\chi_{stB} = (\varepsilon_4 + |\varepsilon_6|)/d_\chi \quad (7)$$

where $d_\chi = 520$ mm is the vertical distance between transducers and ε_i (i = 2, 4, 5 and 6) indicates the average strains obtained from Eq. (1). It is clear From Fig. 11a that plasticization occurred only at the joint section.

The resistance drop in Fig. 10 does not appear in Fig. 11a because the displacement transducers used for curvature measurements at the joint section were removed immediately before the rupture of the projecting bars. A detail of Fig. 11a for $\chi \leq 0.015$ 1/m is reported in Fig. 11b, highlighting the higher deformability of the joint section also for very low bending moments.

4.2.4. Analytical interpretation

For the purpose of comparison with the experimentally determined moment resistance, an estimate of the mean value of the ultimate moment can be obtained by considering, for the joint section, the strain diagram reported in Fig. 12, where the maximum strain for the concrete in compression is assumed to coincide with the average maximum compression strain obtained from the test, i.e., $\varepsilon_{cu} = 0.74\%$. For concrete strength class C50/60, ratio $f_{ck}/f_{ck,cube} = 0.83$. The same value was adopted for ratio $f_{cm}/f_{cm,cube}$ between mean strengths, leading to $f_{cm} = 57$ MPa. For steel, strengths $f_{ym} = 517$ MPa and $f_{tm} = 633$ MPa (Table 2) were assumed. Using standard constitutive relationships (see [30]), strain and stress in the bottom bars turn out to be $\varepsilon_{1a} = 5.18\%$ and $\sigma_{1a} = 566$ MPa, respectively. The resulting neutral axis depth, $y_n = 53$ mm, is lower than the depth at which horizontal cracks were observed in the compression chord after the test, which extended up to the

upper projecting bars. The computed moment resistance, $M_a = 315$ kNm, is lower than the experimental resistance M_m of about 10.5%. In bending tests, a better fit of the analysis results with the experimental data is usually expected when material characteristics are known. In this case, in analogy with the tension test, a reinforcement tensile strength larger than that measured for the steel specimens may explain the discrepancy.

The design moment resistance of the joint section, evaluated for reinforcing steel grade B450C [32] and concrete strength class C50/60, is $M_{Rd} = 208$ kNm. Thus, the system proposed yields an over-strength factor for pure bending equal to $M_m/M_{Rd} = 1.69$.

The significant difference between maximum measured and calculated tensile strains, i.e., 7.70% and 5.18%, respectively, may be caused, also in this case, by the bar slip with respect to the surrounding concrete.

In Fig. 10 the estimated linear elastic load-deflection responses of the specimen for uncracked (dashed line with slope K_I) and cracked concrete (dashed line with slope K_{II}) are reported for comparison with the experimental response. The calculation of stiffnesses K_I and K_{II} is reported in Table A.3 (row headings: Slope of P-u_m response; column heading: MB). The analytical evaluation of stiffnesses taking account of the variations of the reinforcement configuration along the specimen is beyond the scope of this paper. For technical purposes, parameters K_I and K_{II} were referred to cross-section D-D reported in Fig. 1c, representative of the parts of specimen located outside the lap zone.

The horizontal lines labeled $P_{cra} = M_{cra}/a = 62.8$ kN and $P_{ya} = M_{ya}/a = 164.6$ kN in Fig. 10 represent computed cracking and yielding loads, respectively, with $M_{cra} = 87.9$ kNm and $M_{ya} = 230.4$ kNm being the corresponding moments reported in Table A.3 (row headings: Cross-section D-D in Fig. 1c; column heading: MB). Note that the initial stiffness of the experimental behavior is larger than K_I, whereas for $P_{cra} \le P \le P_{ya}$ stiffness K_{II} predicts the actual response accurately.

Stiffnesses K_I and K_{II} of the elastic responses shown in Fig. 11 are reported in Table A.3 (row headings: Slope of M-χ response; column heading: MB). These stiffnesses were calculated for the

joint section, where the average curvature was measured, and refer to uncracked and cracked concrete, respectively. From Fig. 11b it can be noted that, for the cross-section in proximity of the joint section, the bending rigidity coincides with K_I up to the first cracking, and then decreases and tends to approach K_{II}. Conversely, the initial response of the joint section is well approximated by a straight line with slope $0.36K_{II}$.

4.3. Cyclic bending test

4.3.1. Specimen layout and testing protocol

The specimen used for this test was identical to that of the monotonic bending test described in the previous Section. It was installed into the reaction frame and placed on roller supports. The span length was again L = 4 m. A symmetrical four-point bending test configuration was adopted, with each load being applied at a distance a = 1.6 m from the nearest support (Fig. 13a). The choice of using a different value of a with respect to the monotonic bending test was imposed by practical problems, as it will be described in Paragraph 4.3.2.

A total of twelve complete loading cycles and a half were carried out in about four hours. The first five cycles were load-controlled, whereas a displacement control was used for the subsequent cycles. The loading protocol in reported in Fig. 14 (where load is positive when directed downward). For the first three cycles, the total applied load was lying in the range $|2P| \leq 125$ kN defined not to exceed the analytical cracking load. For the fourth and fifth cycles, the total applied load was lying in the range $|2P| \leq 250$ kN defined to attain the analytical load corresponding to yielding of the longitudinal reinforcement. Then, the displacements measured by transducers L9 and L10 were controlled, and two cycles were carried out for each of the following intervals: $|u_9|$, $|u_{10}| \leq$ 15, 25 and 35 mm (cycles from 6th to 11th). These target values were selected based on typical drift values provided in [33] to illustrate the overall structural response associated with various structural performance levels. Drifts $|\theta_i| = |u_i|/a$ (i = 9, 10) computed for $|u_i|$ = 15 and 35 mm are approximately equal to the drift limits for Immediate Occupancy (1%) and Life Safety performance

levels (2%), respectively, whereas $|u_i| = 25$ mm corresponds to an intermediate situation. In the twelfth cycle, the maximum absolute values of the imposed displacement were 48 mm ($|\theta_i| = 3\%$) and 56 mm ($|\theta_i| = 3.5\%$), corresponding to 75% and about 90%, respectively, of the drift limit for Collapse Prevention performance level (4%).

4.3.2. Testing equipment and measuring system

Cyclic bending was achieved using two hydraulic jacks placed at midspan, one on the top and the other on the bottom of the specimen (Fig. 13b). These jacks applied downward and upward loads, respectively. Two load transfer elements were used to apply the jack forces to the cross-sections at $a = 1.6$ m from the end supports. Due to the vertical dimension of the reaction frame, it was necessary to limit the depth of the two load transfer elements. This did not allow for keeping the same configuration as in the monotonic bending test (a larger load-to-load distance would have required deeper load transfer elements). Anyway, this choice did not affect the crack pattern because the damage concentrated at the joint section as in the monotonic bending test (see Paragraph 4.3.3).

The locations of the twelve displacement transducers used to monitor strains and deflections are reported in Fig. 13c. Transducers L1 to L8 (with $b_i = 100$ mm, $i = 1$ to 8) were used to obtain the average curvature at the joint section. Transducers L9 and L10 and transducers L11 and L12 were used to measure deflections under the loads and rigid body displacements of the test specimen, respectively. Views of test specimen and bottom jack are reported in Figs. 15a and 15b, respectively.

4.3.3. Experimental results

The damage concentrated at the joint section and was characterized by yielding and rupture of the bottom projecting bars. Images of the joint section taken during the test are reported in Fig. 16.

The maximum applied load attained in the test was $2P_m$ = 335 kN, resulting in a maximum bending moment $M_m = P_m a$ = 268 kNm.

The plot of the single load applied to the specimen, P, versus net vertical deflection under the load, u_l (i.e., the displacement measured by transducer L10 decreased by the rigid body displacement of the specimen), is reported in Fig. 17, where linear responses for uncracked and cracked concrete, computed for cross-section D-D shown in Fig. 1c, take slopes K_I and K_{II} reported in Table A.3 (row headings: Slope of P-u_l response; column heading: CB). Top horizontal and right vertical axes report drift and moment values, respectively. In the same figure, the red dash-dot curve with solid circles represents the envelope of the hysteresis loops. Some load-deflection pairs of this envelope, together with the corresponding values of drift ($\theta = u_l/a$) and average curvature at the joint section (χ_{joint}), are reported in Table 3. The average curvature was evaluated from the average strains using the following relation (see Fig. 13c):

$$\chi_{joint} = [(\varepsilon_2 + \varepsilon_4)/2 - (\varepsilon_1 + \varepsilon_3)/2]/d_\chi \quad (8)$$

where d_χ = 340 mm is the distance of transducers L1 and L3 to transducers L2 and L4.

In correspondence of the total load $2P$ = 288 kN, corresponding to the computed first yielding load $P_{ya} = M_{ya}/a$ = 144 kN (with M_{ya} being reported in Table A.3, row heading: Cross-section D-D in Fig. 1c; column heading: CB), the measured values of deflection under the load, drift and average curvature resulted to be u_{1y} = 11.1 mm, $\theta_y = u_{1y}/a$ = 0.69% and χ_y = 0.05 1/m, respectively (Table 3).

The bottom projecting bars broke first. This occurrence is emphasized by a sudden resistance drop in Fig. 17. Deflection and curvature at bar failure were u_{lu} = 35 mm (downward) and χ_u = 0.37 1/m, respectively, resulting in ductility ratios u_{1u}/u_{1y} = 3.2 and χ_u/χ_y = 7.4. The corresponding drift value, θ_u = 2.19%, is slightly larger than the allowable limit for Life Safety performance level reported in [33]. Immediately after the rupture of the outer bars, a resistance $2P_u = 0.77(2P_m)$ was recorded. Then, the test was continued up to reach a downward deflection u_1 = 61.5 mm, observing

a slight increase in resistance. The corresponding drift, $\theta = 3.84\%$, is almost twice the limit for Life Safety performance level.

The specimen showed a stable hysteretic behaviour without substantial degradation in the energy dissipation due to pinching.

4.4. Test with combined bending and axial load

4.4.1. Specimen layout and testing protocol

A symmetric four-point bending test configuration was adopted also in this case (Fig. 18a). The specimen was simply-supported and presented a span length of 3.4 m. This span was reduced with respect to the previous two experiments because of the presence, at the specimen end sections, of the anchoring systems needed for the application of the axial load. The load-to-support distance was $a = 1.4$ m as for the monotonic bending test.

The specimen was initially subjected to a compressive axial load $N = 1620$ kN in the absence of lateral forces. This axial load is approximately corresponding to $0.1 f_{cm} A_I$, with $f_{cm} = 0.83 f_{cm,cube}(t) = 57.9$ MPa (Table 1) and $A_I = 0.253$ m^2 (Table A.3). With reference to the design values of the material properties, the initial axial load is also equivalent to $0.2 f_{cd} A_I$, with $f_{cd} = \alpha_{cc} f_{ck}/\gamma_c = 28.3$ MPa ($\alpha_{cc} = 0.85$ and $\gamma_c = 1.5$, see [30]) being the design compressive strength for concrete class C50/60. Whilst undergoing compression, the specimen was subjected to three lateral loading cycles with a force per jack ranging between 0 and 70 kN to check the data acquisition system. This lateral load was selected to preserve concrete uncracked. Then, the loads were increased simultaneously up to failure.

4.4.2. Testing equipment and measuring system

The axial compression was achieved by tensioning twelve 12.5 mm-diameter seven-wire strands, anchored to the specimen end sections by means of two ribbed steel plates. The axial load was

measured by two 1 MN-full scale load cells with nominal sensitivity 2 mV/V (LC1 and LC2 in Fig. 18b) inserted between the end section of stub column A and the relevant anchoring plate.

Six linear displacement transducers (L1 to L6 in Fig. 18b) were used to measure longitudinal strains at the joint section, whereas net deflections under the loads were obtained from the measurements of four transducers (L7 to L10 in Fig. 18b).

A view of the test specimen before the test is reported in Fig. 19a, whereas the central region of the specimen at the beginning of test is shown in Fig. 19b.

4.4.3. Experimental results

The damage mainly affected the joint section (Fig. 20a), where the concrete compression strength was attained. On the specimen top side, a spread of the compression failure within an approximately square region with dimension ≈ 0.5 m was observed at the end of test (Fig. 20b).

The maximum applied load per jack attained in the test and corresponding net mean deflection under the loads were $P_m = 423$ kN and $u_l = 15.65$ mm, respectively. At the same time, from the measurements of load cells LC1 and LC2 an axial load $N = 1741$ kN was obtained. Average maximum tensile strain in the bottom projecting bars obtained from L4 measurements was $\varepsilon_4 = 3.4\%$.

The experimental P-u_l plot is reported in Fig. 21a. In the same figure, the right vertical axis is for the bending moment in the cross-sections where loads were applied. It is worth noting that the end section rotations occurred during the test led to an elongation of the strands, and then to an increase of the axial load measured by the load cells. To account for the second order effects, the bending moment was computed as $M = M_1 + Nu_l$, where $M_1 = Pa$ indicates the first order moment, and Nu_l is the second order contribution. Then, the maximum bending moment attained in the test (for $P = P_m = 423$ kN, $N = 1741$ kN, $u_l = 15.65$ mm) resulted to be $M_m = 619$ kNm.

The experimentally determined plot of the moment versus average curvature at the joint section (χ_{joint}) is reported in Fig. 21b. The average curvature was obtained from the following relation:

$$\chi_{joint} = (\varepsilon_3 + |\varepsilon_5|)/d_\chi \quad (9)$$

where d_χ = 520 mm is the vertical distance between transducers L3 and L5 and ε_i (i = 3, 5) indicates the average strains obtained from transducers measurements divided by b_i = 100 mm (see Fig. 18b).

4.4.4. Analytical interpretation

An estimate of the mean value of the ultimate moment was obtained by considering, for the joint section, the strain diagram reported in Fig. 12. The maximum strain for the concrete in compression was assumed to coincide with the average maximum compression strain obtained from the test, i.e., $\varepsilon_{cu} = \varepsilon_5 = 0.62\%$. Correspondingly, for $N = 1741$ kN, the maximum calculated tensile strain in the projecting bars is $\varepsilon_{1a} = 1.98\%$, leading to tensile stress $\sigma_{1a} = 534$ MPa and neutral axis depth $y_n = 100$ mm, approximately equal to the depth at which the horizontal cracks were observed in the compression chord after the test. The computed moment resistance, M_a = 613 kNm, substantially coincides with bending resistance M_m obtained from the test. Therefore, also in the presence of combined bending and axial load the joint section can develop a bending resistance equivalent to that computed for traditional RC members.

With regard to the design moment resistance computed for axial load N = 1741 kN, assuming design properties for steel grade B450C and concrete strength class C50/60 would yield $\varepsilon_{cu} = 0.35\%$, y_n = 170 mm and M_{Rd} = 460 kNm. Thus, in this case the over-strength factor for the connection is $M_m/M_{Rd} = 1.35$.

The difference between measured (3.40%) and estimated tensile strain (1.98%) in the bottom projecting bars might be due, also in this case, to the bar slip.

In Fig. 21a the estimated linear elastic load-deflection responses of the specimen for uncracked (dashed line with slope K_I) and cracked concrete (dashed line with slope K_{II}) are reported for comparison with the experimental response. The stiffnesses of two straight lines, obtained with reference to cross-section D-D shown in Fig. 1c neglecting the second order effects, are reported in Table A.3 (row headings: Slope of P-u_l response; column heading: AB). In the same figure, the

horizontal lines labeled M_{cra} and M_{ya} refer to cracking and yielding moments reported in Table A.3. It can be noted that the column stiffness can be approximated by a straight line with slope $0.3E_{cm}I_I$, with I_I being the second moment of area for uncracked concrete (Table A.3). This stiffness coincides with that provided in Section 5.8.7 of [30] for cast-in-place columns.

Linear moment-curvature responses reported in Fig. 21b were computed for the joint section, where the average curvature was measured. Their slopes are reported in Table A.3 (row headings: Slope of M-χ response; column heading: AB). Note that, due to the axial compression, the M-χ response for cracked concrete does not pass through the origin. Intercept M_{0a} is reported in Table A.3. The joint section behaves as an uncracked concrete section only for small bending moments. The section deformability increases quickly with the moment, and the local slope of the experimental curve is wherever much lower than K_{II}.

4.5. M-N interaction diagram

The bending moment-axial force interaction diagrams for the joint section, evaluated for design and mean values of reinforcing steel and concrete strengths, are reported in Fig. 22, where a negative axial load means tension. Typical parabola-rectangle and linear-hardening elastic-plastic constitutive relationships were used for concrete and reinforcing steel, respectively. In particular, the design strengths were related to concrete strength class C50/60 and steel grade B450C. With regard to the mean values of the material properties, compression strength f_{cm} = 57.0 MPa, strain at the attainment of the maximum stress ε_{c2} = 0.2%, and ultimate strain ε_{cu2} = 0.7% were adopted for the concrete in compression, whereas, for the reinforcing steel, yield and ultimate strengths f_{ym} and f_{tm} reported in Table 2 were adopted. The four solid circles in Fig. 22 indicate the M-N pairs obtained at failure from the tests described in Sections 4.1 to 4.4. The figure confirms that ultimate resistances of precast columns with grouted sleeve connections can be estimated using standard calculations for cast-in-place columns.

4.6. Shear test

The test was aimed at verifying the shear load-carrying capacity of the grouted sleeve connection, particularly at the joint section.

4.6.1. Specimen layout and testing protocol

The test configuration for the shear test is shown in Fig. 23a. The specimen was simply supported in correspondence of two sections, one located in stub column A at 0.1 m from the joint section, and the other in stub column B at 1 m from the joint section itself. Two vertical point forces, F_1 and F_2, were applied to the specimen top side at 0.1 m and 1 m from the joint section, respectively (Fig. 24). To reduce the contribution to the shear resistance due to friction, the grout used at the joint section to seal the interface gap between the column units was preliminarily removed for a depth of 25 mm.

Because of the isostatic nature of the test configuration (Fig. 24), shear force V_j and bending moment M_j at the joint section, ignoring the specimen self weight, can readily be obtained in the form:

$$V_j = 9/11\ (F_1 + F_2) \tag{10}$$

$$M_j = 0.9/11\ (F_1 - 10F_2) \tag{11}$$

Equation (11) yields M_j in kNm if F_1 and F_2 are expressed in kN.

There was interest in investigating a possible shear strength degradation under cyclic loading. Five loading-unloading cycles were then carried out prior to attain failure. The target values of F_1 and F_2 in the first cycle were selected to give $V_j = 639$ kN, a value exceeding by 30% the design shear resistance of the joint. This resistance was estimated with reference to the recommendations reported in [30] for concretes cast at different times. For a smooth interface, the contribution due to the reinforcement that crosses the interface is given by:

$$V_{Rds} = 0.5 A_s f_{yd} \tag{12}$$

that for the eight 20 mm-diameter reinforcing bars leads to V_{Rds} = 490 kN (= 639/1.3). In the second loading cycle, the target value V_j = 711 kN (= 1.45V_{Rds}) was attained. In the subsequent cycles, the ultimate shear resistance of the joint section was attained and kept until failure.

4.6.2. Testing equipment and measuring system

Hydraulic jacks with nominal capacity 1 MN and 100 kN were used to reproduce forces F_1 and F_2, respectively. The forces were measured by means of pressure transducers with nominal capacity 700 bar connected in series with the oleodynamic circuit. Force F_2 was also measured using a 100 kN-full scale load cell with nominal sensitivity 2 mV/V.

Nine linear displacement transducers (see Fig. 23b) were used to measure: relative displacements experimented by the projecting bars (L1 to L4) and the two stub columns (L5 and L8); absolute deflections at the joint section (L6 and L9) and at the point of application of F_2 (L7). A detail view of the specimen before the test is shown in Fig. 25a.

4.6.3. Experimental results

The damage concentrated at the joint section (Fig. 25b), were shear yielding of the projecting bars occurred.

The experimentally determined plot of V_j versus vertical relative displacement u_r between the stub columns (measured by transducer L5) is reported in Fig. 26. The maximum value of V_j obtained from the test is V_{jm} = 747 kN, corresponding to M_j = 5.7 kNm. The relative displacement needed for developing shear resistance V_{Rds} = 490 kN (Eq. (12)) was u_r = 1.2 mm = 0.06$\varnothing_b$, with $\varnothing_b$ = 20 mm being the bar diameter. The maximum achieved relative displacement was u_r = 26 mm.

4.6.4. Analytical interpretation

According with [34], the maximum shear force that can be transferred from the eight projecting bars is given by the following expression:

$$V_{ja} = A_s f_{ym}/\sqrt{3} = 749 \text{ kN} \quad (13)$$

where A_s = 2512 mm^2 (Table A.1) and mean yield strength f_{ym} = 517 MPa (Table 2) is used in analogy with the previously presented tests' interpretations. Note that maximum shear V_{jm} = 747 kN attained in the test substantially coincides with the pure shear resistance provided by Eq. (13).

The formulations usually adopted in the literature to evaluate the design shear resistance of dowelled connections take account of failure mechanisms involving, in addition to bar yielding, the contribution of the concrete strength [14, 35]. The resulting capacity is proportional to the square root of the product between steel and concrete strengths and is significantly lower (normally around 50%) than that associated with the pure shear mechanism (Eq. (13)). The proposed connection seems then able to develop the upper bound of the shear resistance. Probably, the closely spaced transverse reinforcement was effective in avoiding premature brittle concrete failure.

5. DISCUSSION AND CONCLUSIONS

The experimental characterization of a grouted sleeve connection for precast RC columns was presented. The precast column units had square cross-section with the side of 500 mm and were connected with one another by lap-splicing the longitudinal reinforcing bars. The eight 20 mm-diameter bars protruding from one unit were inserted into the corrugated steel sleeves arranged in the other unit, and then grouted. In all tests, the loads were applied statically. It is worth underlining that no standard (monolithic) column has been tested in this testing program. For comparison with the experimental results, the behavior of a standard RC column, with the same reinforcement as the joint section of the proposed connection system, was estimated by calculation.

The direct tension test highlighted the effectiveness of the stress transfer along the splice region. Failure took place far from the joint section, outside the bar splice region.

In monotonic bending tests, with and without axial compression, failure occurred at the joint section placed at specimen midspan, with yielding and rupture of the projecting bars. With respect to the design bending resistance computed in accordance with the rules for traditional RC members,

the joint section showed an over-strength factor of 1.69 and 1.35 in the case of pure bending and combined axial load and bending, respectively. In terms of deformability, the tests showed a clear distinction between local and global responses. Moment-curvature diagrams for the joint section, obtained from load and strain measurements, indicate a higher deformability in comparison with those computed for equally reinforced RC sections, probably because of the slip experienced by the projecting bars. Conversely, load-deflection plots do not show any significant reduction of the global stiffness with respect to conventional columns. For the specimen subjected to combined bending and axial compression, the bending stiffness after cracking is well approximated by $0.3E_{cm}I_I$ (see Fig. 21a), coinciding with the stiffness provided by Eurocode 2 for cast-in-place columns in the presence of second-order effects (see [30], Eqs. (5.21) and (5.26) with a zero creep coefficient).

In the shear test, the shear force resisted by the joint section was substantially coincident with the pure shear resistance of the eight projecting bars that cross the joint. The failure was again restricted to the joint section.

In the cyclic bending test with zero axial load an over-strength factor of 1.29 was achieved with respect to the computed design resistance and a drift of 3.84%, was attained. Even after the rupture of the outer projecting bars, a stable hysteretic behavior was observed, with almost constant energy dissipation and no evidence of pinching.

Therefore, the experimental evidence enables to state that the proposed connection system for precast columns, designed in accordance with the provisions given in [30], is effective in terms of Ultimate Limit State capacity. The same connection system, but used for a column-to-foundation joint tested in cyclic bending combined with axial compression, will be the subject of a subsequent research.

ACKNOWLEDGEMENTS

The present investigation was developed in the framework of the Research Program FAR 2014 of the University of Ferrara. Moreover, the analyses were carried out within the activities of the (Italian) University Network of Seismic Engineering Laboratories–ReLUIS in the research program funded by the (Italian) National Civil Protection– Progetto Esecutivo 2016 – Research Line "Reinforced Concrete Structures", WP2. The test specimens were provided by Prefabbricati Morri srl in Rimini, Italy. Special acknowledgement is due to Dr. Luisfilippo Lanza for his contribution to the preparation of the experimental tests.

APPENDIX

This appendix reports the calculations of the linear elastic responses shown in Figs. 7, 10, 11, 17 and 21. For geometrical quantities used in the calculations see Table A.1. Analytical relationships for the specimen in axial tension and for those subjected to bending with and without axial compression are reported in Tables A.2 and A.3, respectively.

REFERENCES

[1] International Federation for Prestressing (FIP). *FIP handbook on practical design: Examples of the design of concrete structures*. London: Thomas Telford; 1990.

[2] Bruggeling ASG, Huyghe GF. *Prefabrication with Concrete*. Rotterdam: Balkema; 1991.

[3] International Federation for Prestressing (FIP). *Planning and design handbook on precast building structures*. London: SETO; 1994.

[4] Centre for Advanced Engineering (CAE). *Guidelines for the use of precast concrete in buildings*. 2nd ed. Christchurch: University of Canterbury; 1999.

[5] Elliott KS. *Precast Concrete Structures*. Oxford: Butterworth-Heinemann; 2002.

[6] International Federation for Structural Concrete (FIB). *Seismic design of precast concrete building structures*. FIB Bulletin No. 27. Lausanne: FIB; 2003.

[7] Precast/Prestressed Concrete Institute (PCI). *PCI Design Handbook: Precast and Prestressed Concrete*. 6th ed. Chicago: Precast/Prestressed Concrete Institute; 2004.

[8] International Federation for Structural Concrete (FIB). *Structural connections for precast concrete buildings. Guide to good practice*. FIB Bulletin No. 43. Lausanne: FIB; 2008.

[9] Savoia M, Mazzotti C, Buratti N, Ferracuti B, Bovo M, Ligabue V, Vincenzi. Damages and collapses in industrial precast buildings after the Emilia earthquake. *Ingegneria Sismica-International Journal of Earthquake Engineering* 2012; 29(2-3): 120–131.

[10] Minghini F, Ongaretto E, Ligabue V, Savoia M, Tullini N. Observational failure analysis of precast buildings after the 2012 Emilia earthquakes. *Earthquakes and Structures* 2016; 11(2): 327-346.

[11] Toniolo G. European research on seismic behaviour of precast structures. In: *Proceedings of the 2012 Annual Conference of the New Zealand Society for Earthquake Engineering (NZSEE)*. Christchurch, April 13-15, 2012.

[12] Zoubek B, Isakovic T, Fahjan Y, Fischinger M. Cyclic failure analysis of the beam-to-column dowel connections in precast industrial buildings. *Engineering Structures* 2013; 52: 179–191. DOI: http://dx.doi.org/10.1016/j.engstruct.2013.02.028.

[13] Zoubek B, Fischinger M, Isakovic T. Estimation of the cyclic capacity of beam-to-column dowel connections in precast industrial buildings. *Bull Earthquake Eng* 2015; 13(7): 2145–2168. DOI: 10.1007/s10518-014-9711-0.

[14] Negro P, Toniolo G (eds.). *Design guidelines for connections of precast structures under seismic actions*. EUR - Scientific and Technical Research Reports. JRC Publication No. JRC71599. Publications Office of the European Union; 2012. DOI: 10.2777/37605.

[15] Park R. Perspective on the Seismic Design of Precast Concrete Structures in New Zealand. *PCI Journal* 1995; 40(3): 40–60.

[16] Restrepo JI, Park R, Buchanan AH. Tests on connections of earthquake resisting precast reinforced-concrete perimeter frames of buildings. *PCI Journal* 1995; 40(4): 44–61.

[17] Restrepo JI, Park R, Buchanan AH. Design of connections of earthquake resisting precast reinforced-concrete perimeter frames. *PCI Journal* 1995; 40(5): 68–80.

[18] Parastesh H, Hajirasouliha I, Ramezani R. A new ductile moment-resisting connection for precast concrete frames in seismic regions: An experimental investigation. *Engineering Structures* 2014; 70: 144–157. DOI: http://dx.doi.org/10.1016/j.engstruct.2014.04.001.

[19] O'Leary AJ. Multistory Precast Concrete Framed Buildings. In: *Proceedings of the Tom Paulay Symposium, "Recent Developments in Lateral Force Transfer in Buildings"*. La Jolla, September 20-22, 1993. *Special Publication of the American Concrete Institute* 1995; SP157-10: 211–230. DOI: 10.14359/1016.

[20] Kuttab AS, Dougill JW. Grouted and doweled jointed precast concrete columns - Behaviour in combined bending and compression. *Magazine of Concrete Research* 1988; 40(144): 131–142.

[21] Zheng LX. Grouted precast concrete column connections under reversed cyclic bending and compression. *ACI Structural Journal* 1996; 93(3): 247–256.

[22] Lin CM, Restrepo JI, Park R. Seismic design and behaviour of reinforced concrete beam-column joints. *Research Report 2000-1, Department of Civil Engineering, University of Canterbury, Christchurch*; 2000.

[23] Riva P. Seismic Behaviour of Precast Column-to-foundation Grouted Sleeve Connections. In: Pandey M, Xie W-C, Xu L (eds.). Advances in Engineering Structures, Mechanics & Construction. *Solid Mechanics and Its Applications* 2006; 140: 121–128. DOI: 10.1007/1-4020-4891-2_10.

[24] Riva P, Belleri A. Seismic behaviour of precast column-to-foundation grouted sleeve connections. In: *Proceedings of the First European Conference on Earthquake Engineering and Seismology*. Geneva, September 3-8, 2006.

[25] Belleri A, Riva P. Seismic performance and retrofit of precast concrete grouted sleeve connections. *PCI Journal* 2012; 57(1): 97–109.

[26] Popa V, Papurcu A, Cotofana D, Pascu R. Experimental testing on emulative connections for precast columns using grouted corrugated steel sleeves. *Bull Earthquake Eng* 2014. DOI: 10.1007/s10518-014-9715-9.

[27] Metelli G, Beschi C, Riva P. Cyclic behaviour of a column to foundation joint for concrete precast structures. *European Journal of Environmental and Civil Engineering* 2011; 15(9): 1297–1318. DOI: 10.3166/EJECE.15.1297-1318.

[28] Buratti N, Bacci L, Mazzotti C. Seismic behaviour of grouted sleeve connections between foundations and precast columns. In: *Proceedings of the 2nd European Conference on Earthquake Engineering and Seismology*. Istanbul, August 25-29, 2014.

[29] National Cooperative Highway Research Program (NCHRP). Application of Accelerated Bridge Construction Connections in Moderate-to-High Seismic Regions. NCHRP Report 698. 2011.

[30] European Committee for Standardization. *EN 1992-1-1:2004, Eurocode 2 – Design of concrete structures – Part 1-1: General rules and rules for buildings*. Brussels, Belgium, 2004.

[31] LabVIEW 2015 Help (2015), National Instruments. Available at http://www.ni.com/support.

[32] Italian Ministry of Infrastructure and Transport. *Italian Building Code-D.M. 14/01/2008*. Rome, Italy, 2008 [in Italian].

[33] Federal Management Emergency Agency. *FEMA 356 – Prestandard and commentary for the seismic rehabilitation of buildings*. Washington, D.C., 2000.

[34] International Federation for Structural Concrete (FIB). *fib Model Code for Concrete Structures 2010*. Berlin: Wilhelm Ernst & Sohn; 2013.

[35] Vintzeleou EN, Tassios TP. Behavior of dowels under cyclic deformations. *ACI Structural Journal* 1987; 84(1): 18–30.

Figure Captions

Fig. 1. Typical specimen for tests on the column-to-column grouted sleeve connection: (a) solid view; (b) side view of the reinforcement details and (c) column cross-sections. Dimensions in mm.

Fig. 2. Reinforcement cages for the precast column units: (a) stub columns A and (b) B; (c) detail view of stub column B showing the projecting bars and stirrups along the splice region.

Fig. 3. Comparison between different reinforcement configurations: cross-section (a) along the splice region of the proposed connection (cross-section C-C in Fig. 1c) and (b) at the column base for the column-to-foundation connection investigated in [26]. Dimensions in mm.

Fig. 4. Assemblage of two precast column units: (a) frontal view showing, in one side of stub column A, the holes corresponding to the top end of the sleeves to be grouted and (b) detail view of the insertion of the projecting bars.

Fig. 5. Direct tension test: (a) reinforcement layout (plan view) and (b) locations of the measurement devices. Dimensions in mm.

Fig. 6. Direct tension test: (a) specimen at the beginning of test and (b) crack pattern at the end of test in the zone where the rupture of the reinforcing bars occurred.

Fig. 7. Direct tension test: axial load versus strains measured (a) at the joint section and (b) along the lap splice of stub column A.

Fig. 8. Four-point bending test: (a) test setup (side view) and (b) locations of the linear displacement transducers. Dimensions in mm.

Fig. 9. Four-point bending test: (a) test setup and (b) damage state at the end of test.

Fig. 10. Four-point bending test: load per each jack and corresponding bending moment versus midspan deflection.

Fig. 11. Four-point bending test: (a) moment-curvature plots for the joint section (χ_{joint}) and for a cross-section located in the constant moment region of stub column B (χ_{stB}); (b) detail of the same plots for $\chi \leq 0.015$ 1/m.

Fig. 12. Strain diagram for the joint section.

Fig. 13. Cyclic bending test: (a) test setup and (b) its schematic representation; (c) locations of the linear displacement transducers. Dimensions in mm.

Fig. 14. Cyclic bending test, loading protocol.

Fig. 15. Cyclic bending test: (a) lateral view of the test setup and (b) detail of the bottom jack.

Fig. 16. Cyclic bending test: joint damage observed during the (a) tenth and (b) last downward half cycles for u_l = 35 and 46 mm, respectively, and (c) at the end of test (see solid circles in Fig. 14).

Fig. 17. Cyclic bending test: single applied load (half of the load applied by each jack) and corresponding bending moment versus deflection under the load and drift. Red dash-dot curve with symbols represents the envelope reported in Table 3.

Fig. 18. Test with combined bending and axial load: (a) test setup (side view) and (b) locations of the linear displacement transducers. Dimensions in mm.

Fig. 19. Test with combined bending and axial load: (a) lateral and (b) detail views of the specimen before the test.

Fig. 20. Test with combined bending and axial load, specimen at the end of test: (a) lateral view of the joint section and (b) detail of the central region of the specimen top side.

Fig. 21. Test with combined bending and axial load: (a) load per each jack and corresponding bending moment versus mean deflection under the load; (b) moment-curvature plot for the joint section.

Fig. 22. *M*-*N* interaction diagram for the joint section. Acronyms T, MB, CB and AB stand for Tension, Monotonic Bending, Cyclic Bending and combined Axial load and Bending, respectively.

Fig. 23. Shear test: (a) test setup (side view) and (b) locations of the linear displacement transducers. Dimensions in mm.

Fig. 24. Statically determinate configuration adopted for the shear test. Dimensions in mm.

Fig. 25. Shear test: detail views of (a) test setup and (b) joint section at the end of test.

Fig. 26. Shear test: plot of the shear force versus vertical relative displacement at the joint section.

Table Captions

Table 1. Concrete and grout compressive strengths obtained from tests on cubic specimens.

Table 2. Mean values of the mechanical properties for reinforcing steel.

Table 3. Points of the envelope diagrams obtained from the cyclic bending test: values of jack half-load (P), deflection under the load (u_l), drift (θ) and curvature (χ).

Table A.1. Parameters used in Tables A.2 and A.3.

Table A.2. Specimen subjected to axial tension. Evaluation of the slopes of N-ε linear responses for uncracked concrete (UC) and reinforcing bars (see Fig. 7).

Table A.3. Specimens subjected to monotonic bending (MB), cyclic bending (CB) and combined axial compression and bending (AB). Evaluation of the slopes of P-u_m, P-u_l and M-χ linear responses for uncracked (UC) and cracked concrete (CC).

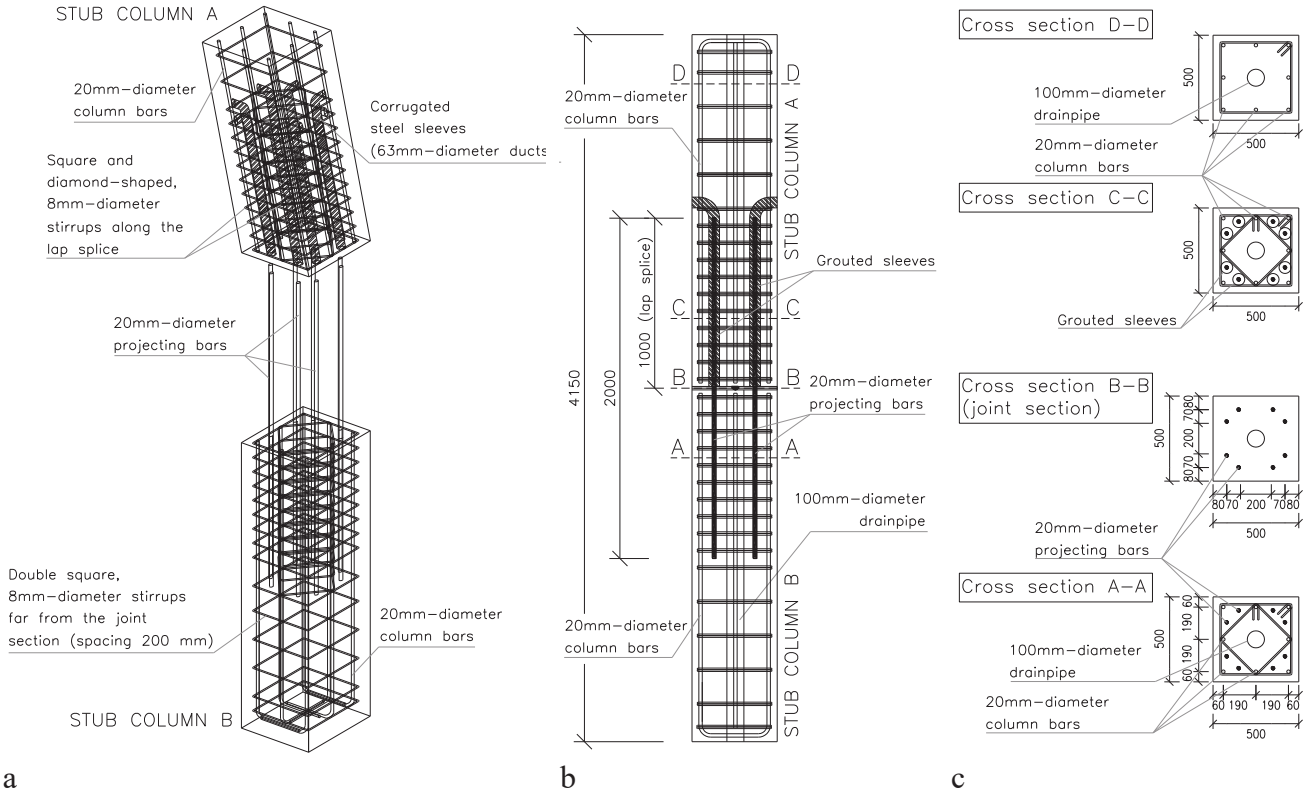

Fig. 1. Typical specimen for tests on the column-to-column grouted sleeve connection: (a) solid view; (b) side view of the reinforcement details and (c) column cross-sections. Dimensions in mm.

Fig. 2. Reinforcement cages for the precast column units: (a) stub columns A and (b) B; (c) detail view of stub column B showing the projecting bars and stirrups along the splice region.

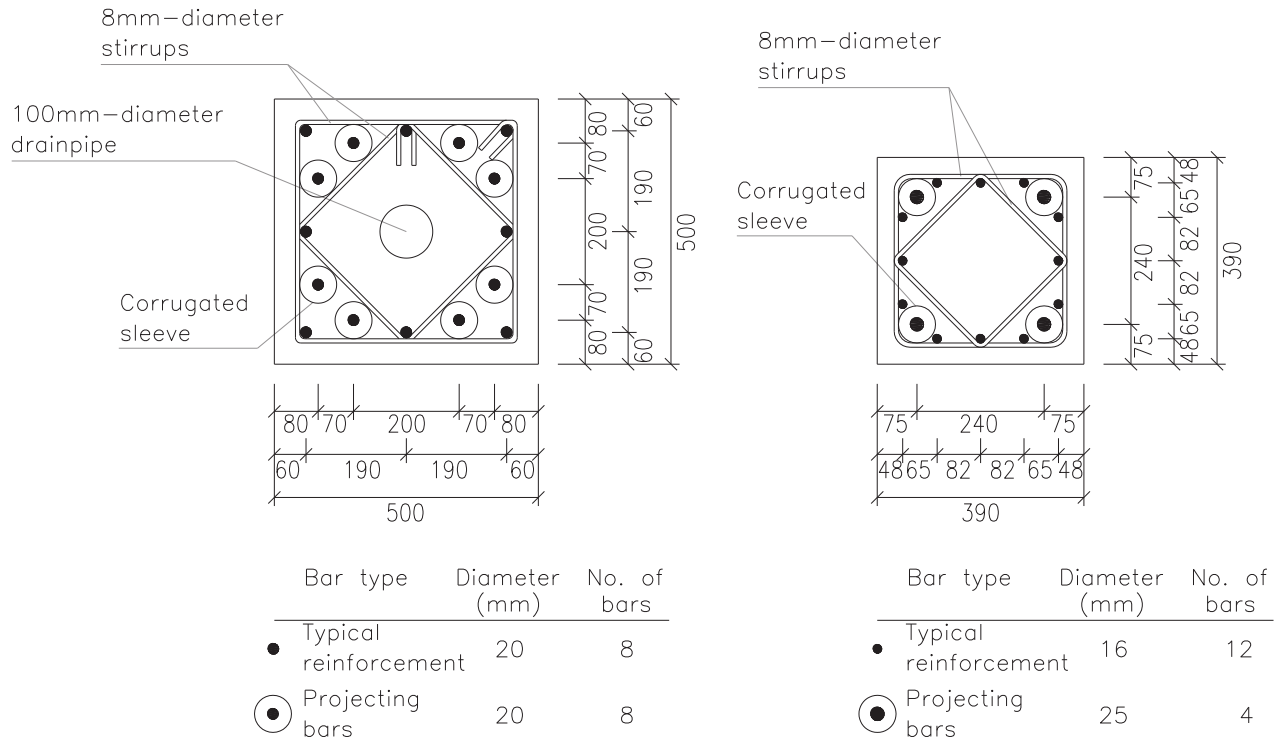

Fig. 3. Comparison between different reinforcement configurations: cross-section (a) along the splice region of the proposed connection (cross-section C-C in Fig. 1c) and (b) at the column base for the column-to-foundation connection investigated in [26]. Dimensions in mm.

a b

Fig. 4. Assemblage of two precast column units: (a) frontal view showing, in one side of stub column A, the holes corresponding to the top end of the sleeves to be grouted and (b) detail view of the insertion of the projecting bars.

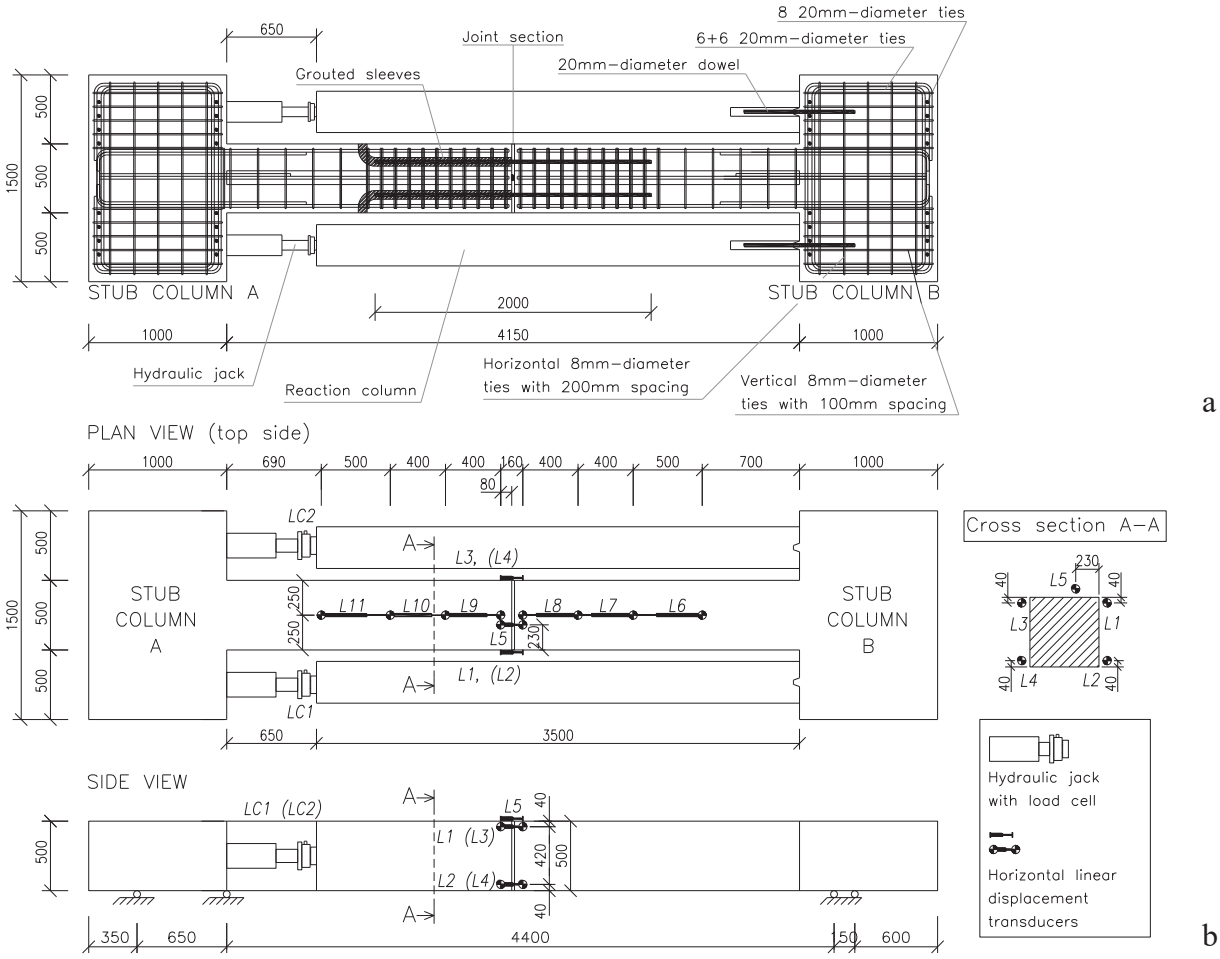

Fig. 5. Direct tension test: (a) reinforcement layout (plan view) and (b) locations of the measurement devices. Dimensions in mm.

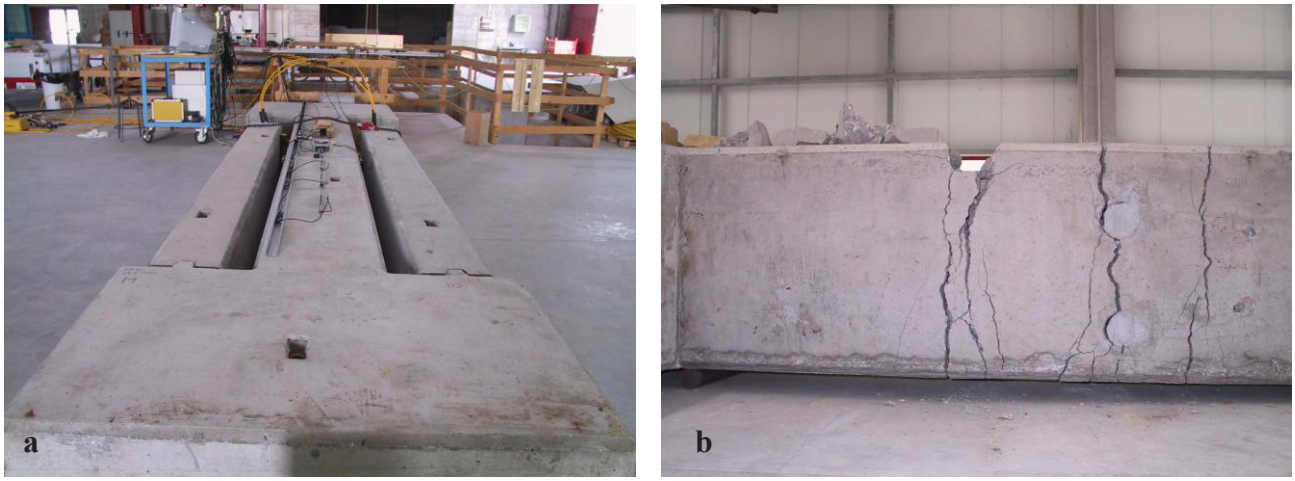

Fig. 6. Direct tension test: (a) specimen at the beginning of test and (b) crack pattern at the end of test in the zone where the rupture of the reinforcing bars occurred.

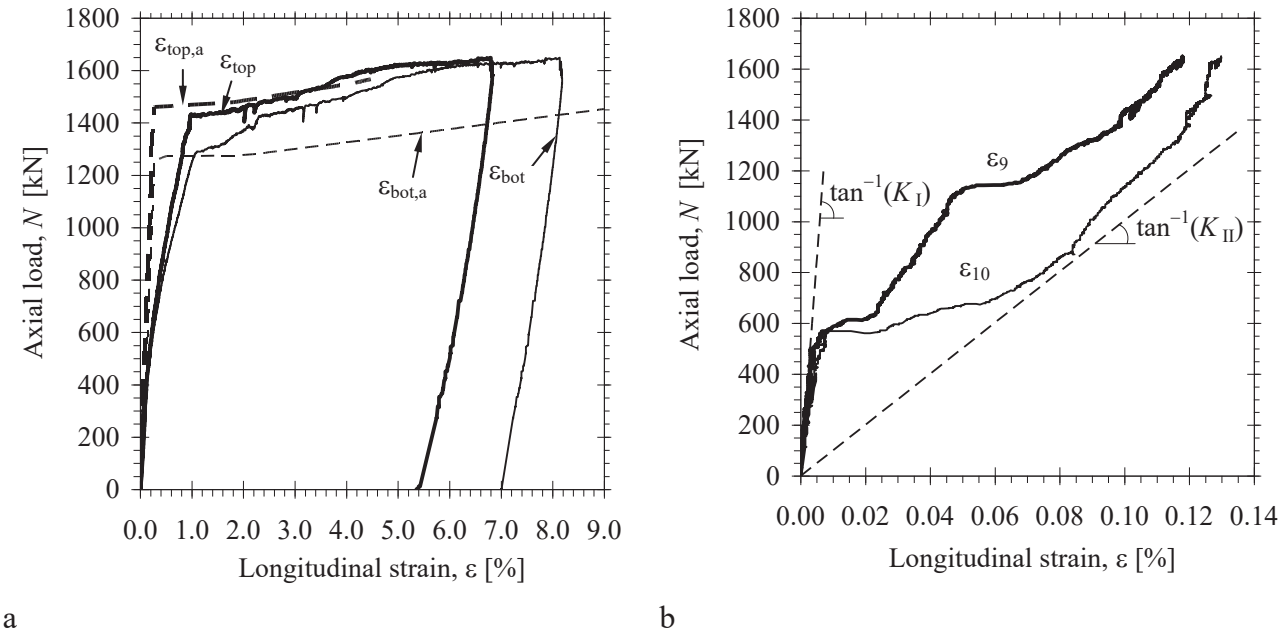

Fig. 7. Direct tension test: axial load versus strains measured (a) at the joint section and (b) along the lap splice of stub column A.

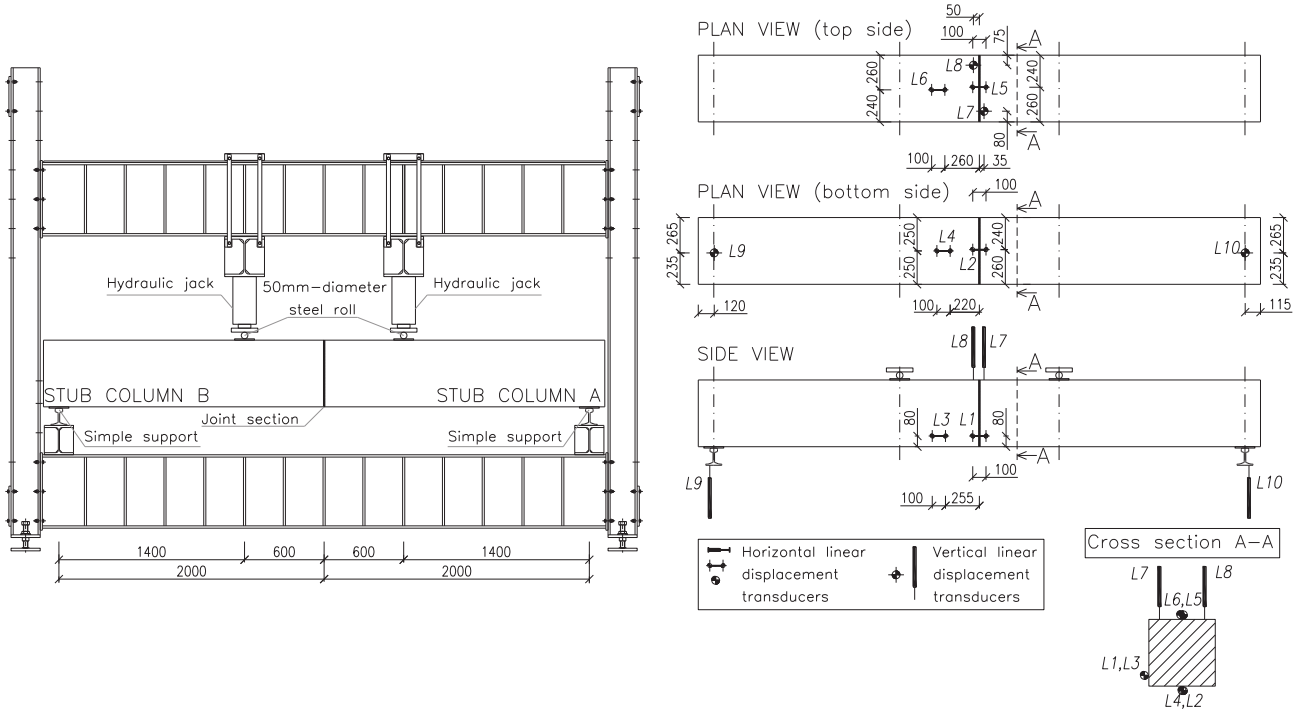

a b

Fig. 8. Four-point bending test: (a) test setup (side view) and (b) locations of the linear displacement transducers. Dimensions in mm.

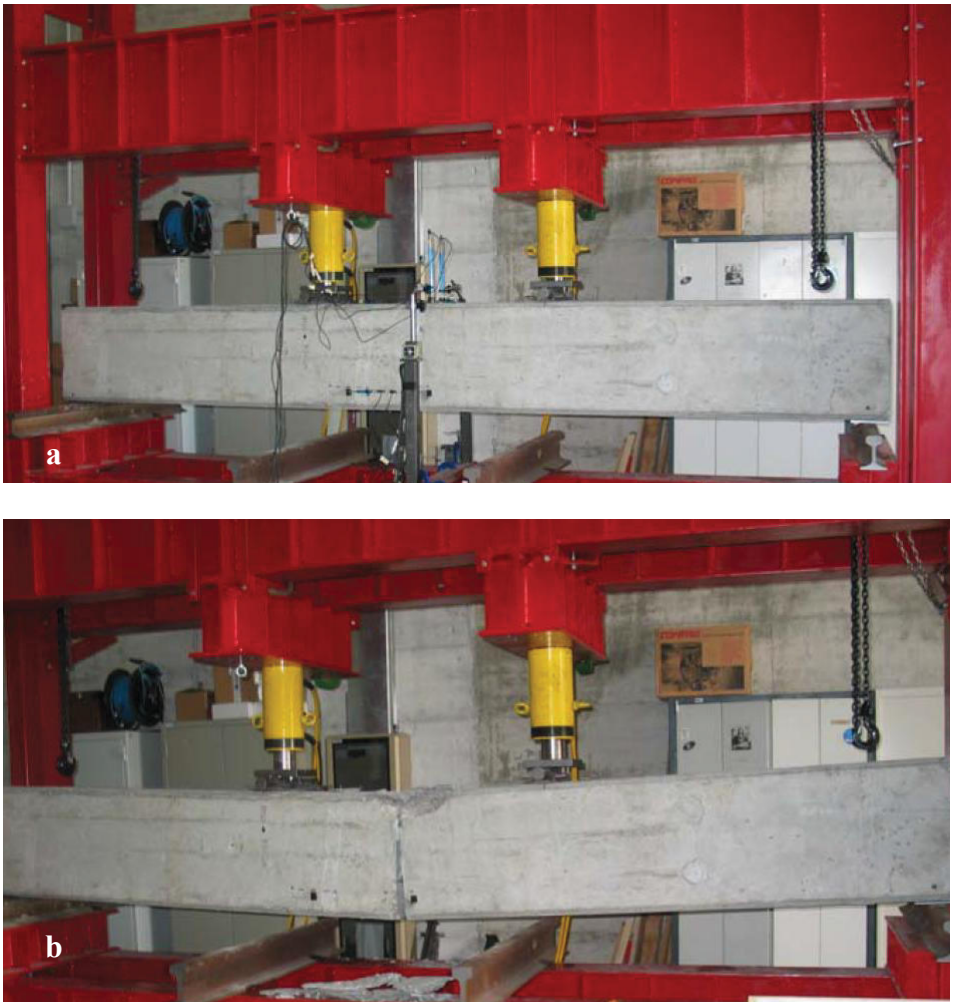

Fig. 9. Four-point bending test: (a) test setup and (b) damage state at the end of test.

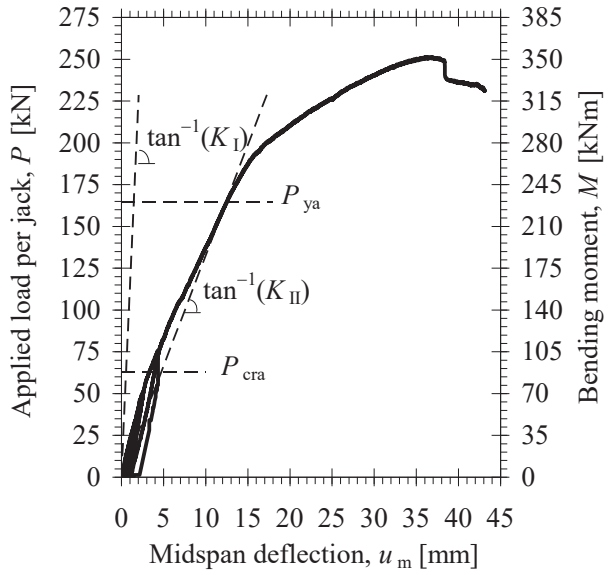

Fig. 10. Four-point bending test: load per each jack and corresponding bending moment versus midspan deflection.

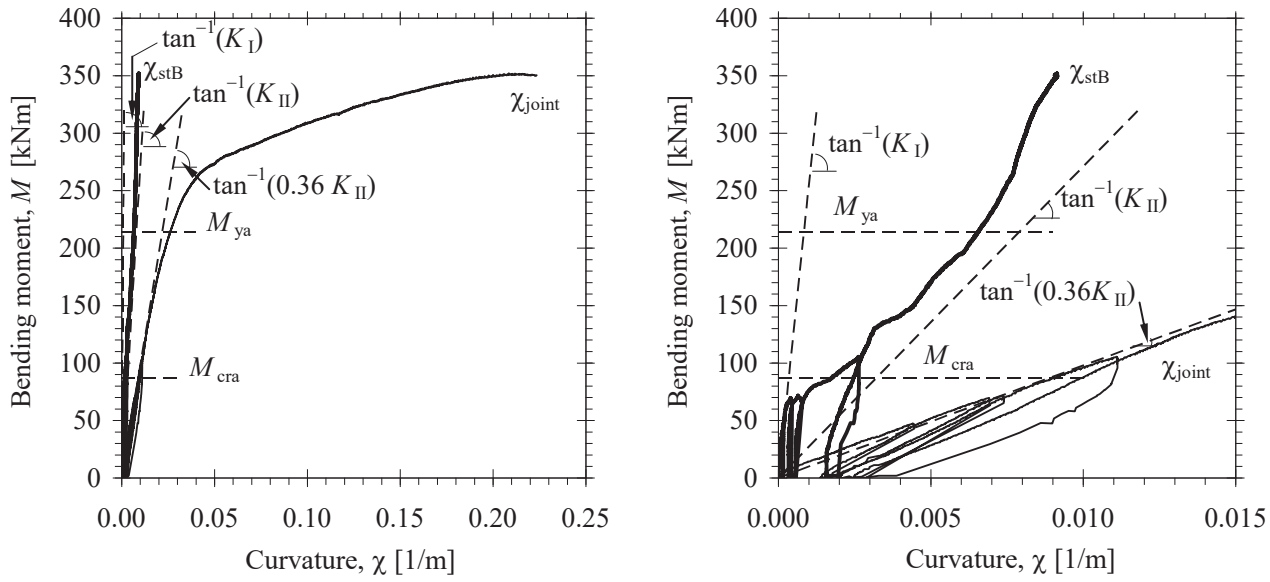

Fig. 11. Four-point bending test: (a) moment-curvature plots for the joint section (χ_{joint}) and for a cross-section located in the constant moment region of stub column B (χ_{stB}); (b) detail of the same plots for $\chi \leq 0.015$ 1/m.

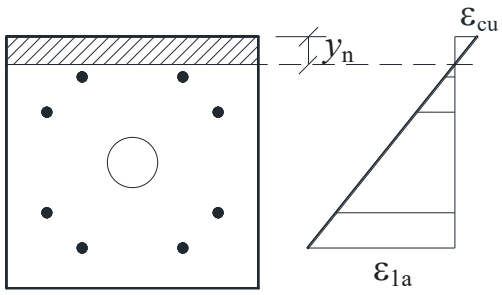

Fig. 12. Strain diagram for the joint section.

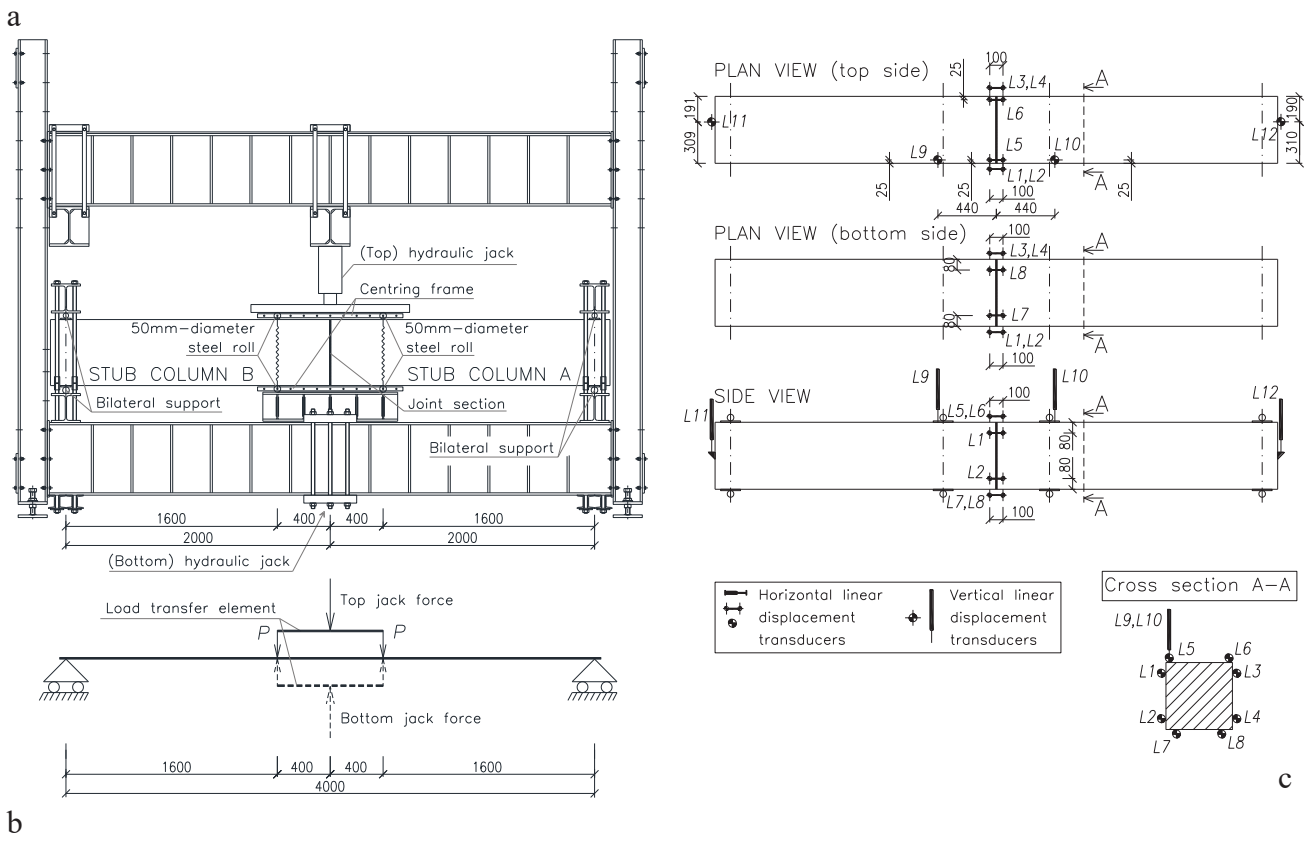

Fig. 13. Cyclic bending test: (a) test setup and (b) its schematic representation; (c) locations of the linear displacement transducers. Dimensions in mm.

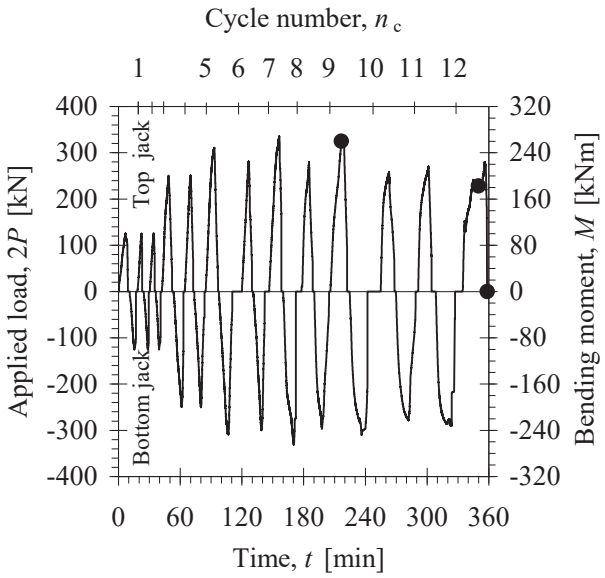

Fig. 14. Cyclic bending test, loading protocol.

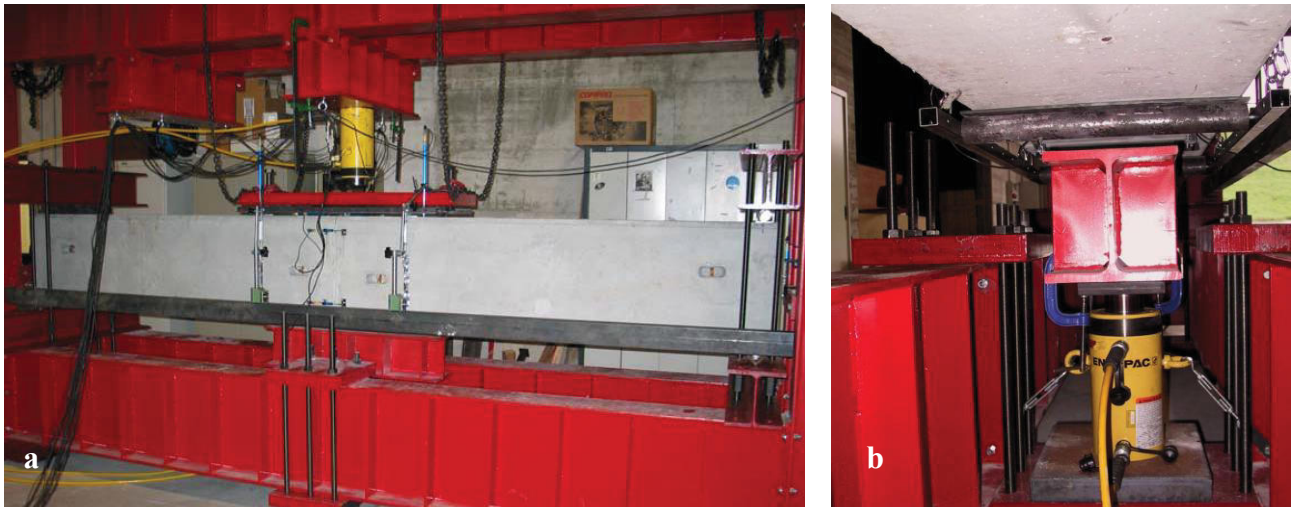

Fig. 15. Cyclic bending test: (a) lateral view of the test setup and (b) detail of the bottom jack.

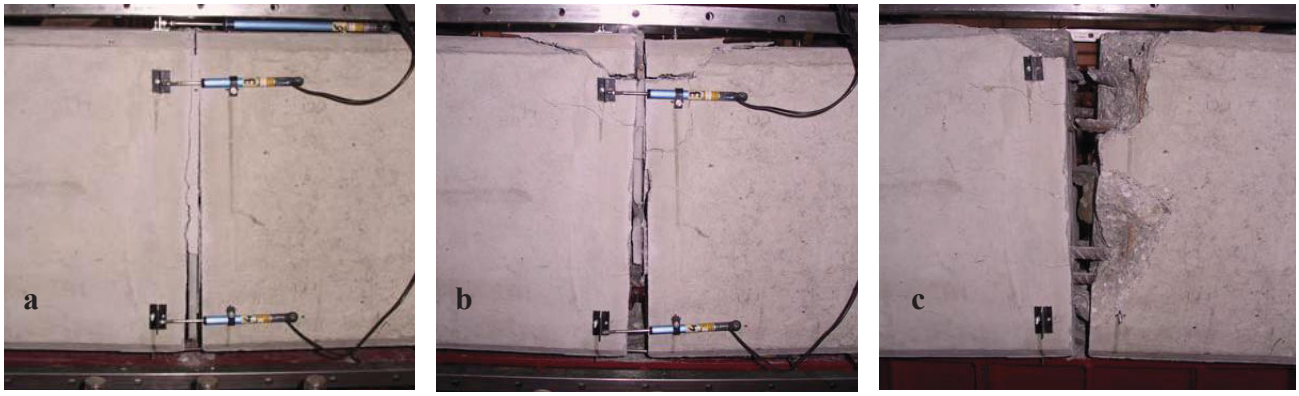

Fig. 16. Cyclic bending test: joint damage observed during the (a) tenth and (b) last downward half cycles for u_1 = 35 and 46 mm, respectively, and (c) at the end of test (see solid circles in Fig. 14).

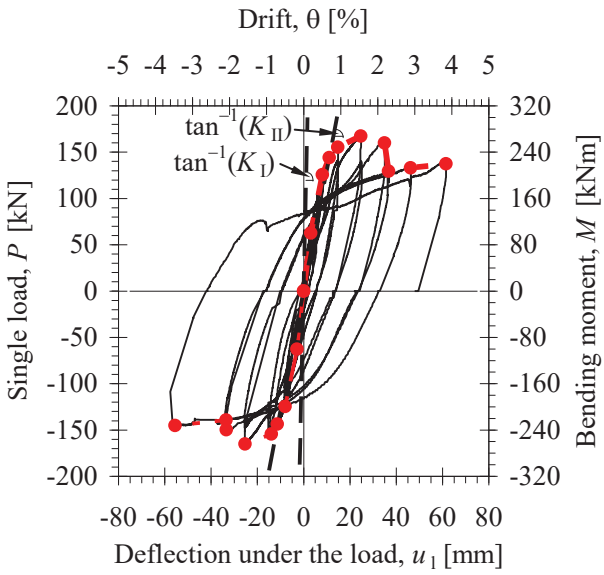

Fig. 17. Cyclic bending test: single applied load (half of the load applied by each jack) and corresponding bending moment versus deflection under the load and drift. Red dash-dot curve with symbols represents the envelope reported in Table 3.

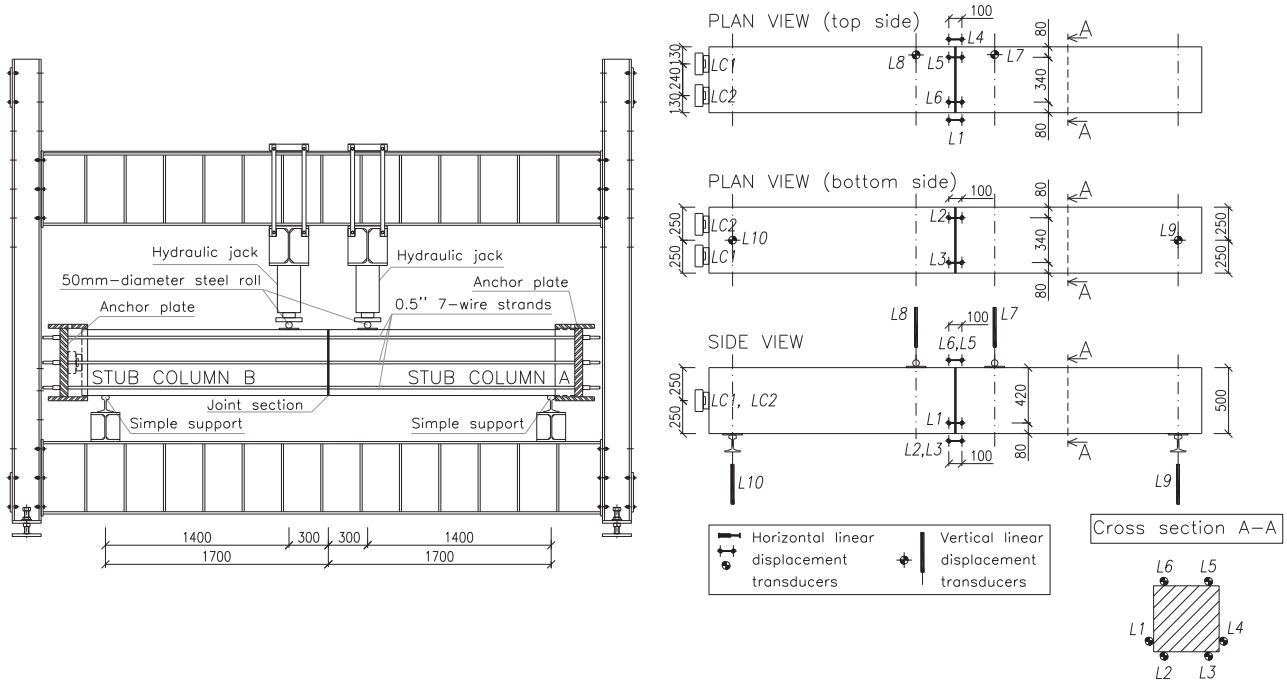

a b

Fig. 18. Test with combined bending and axial load: (a) test setup (side view) and (b) locations of the linear displacement transducers. Dimensions in mm.

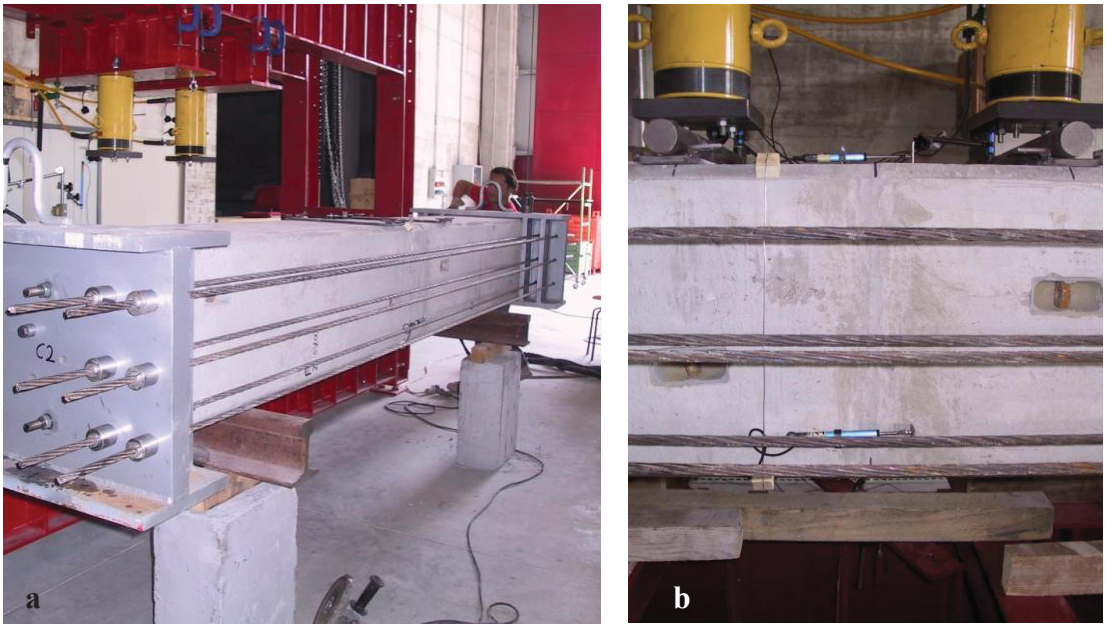

Fig. 19. Test with combined bending and axial load: (a) lateral and (b) detail views of the specimen before the test.

Fig. 20. Test with combined bending and axial load, specimen at the end of test: (a) lateral view of the joint section; and (b) detail of the central region of the specimen top side.

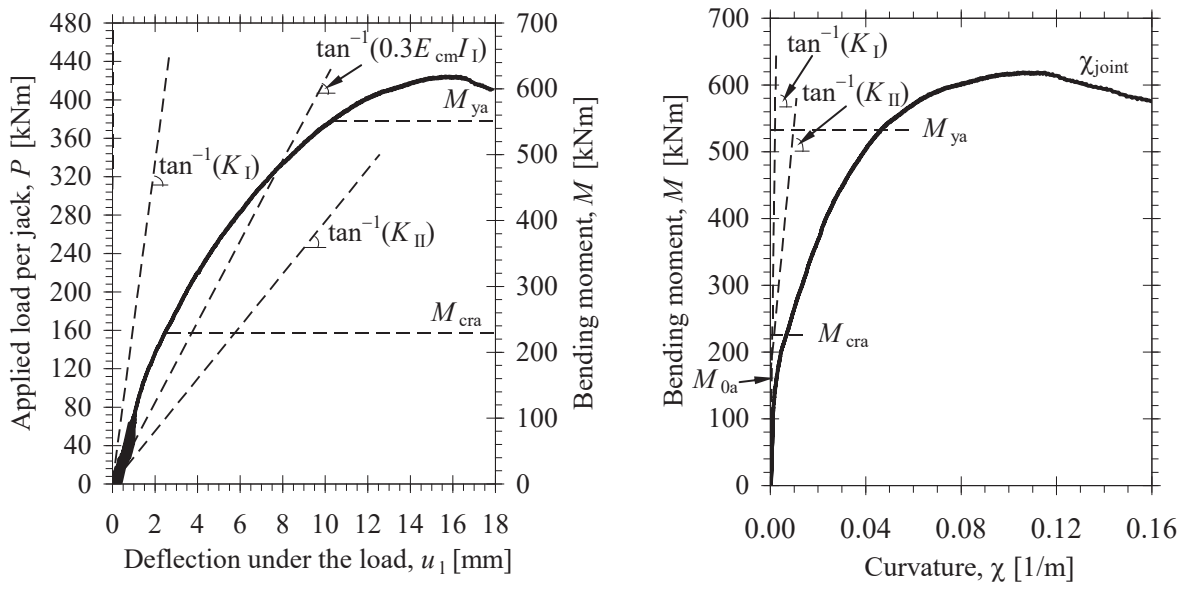

a b

Fig. 21. Test with combined bending and axial load: (a) load per each jack and corresponding bending moment versus mean deflection under the load; (b) moment-curvature plot for the joint section.

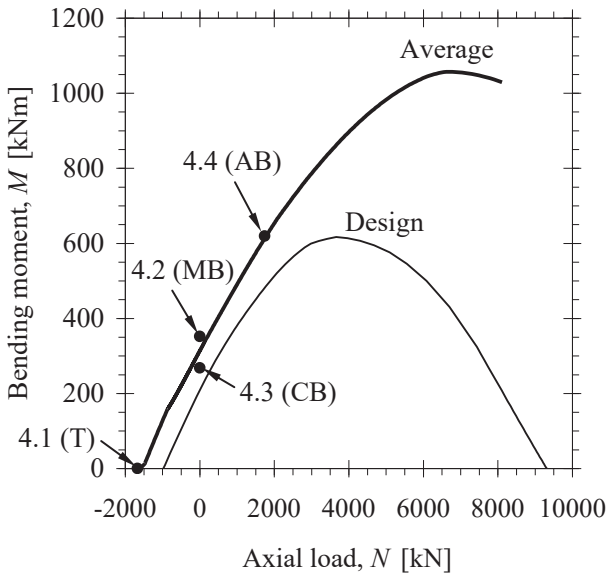

Fig. 22. *M*-*N* interaction diagram for the joint section. Acronyms T, MB, CB and AB stand for Tension, Monotonic Bending, Cyclic Bending and combined Axial load and Bending, respectively.

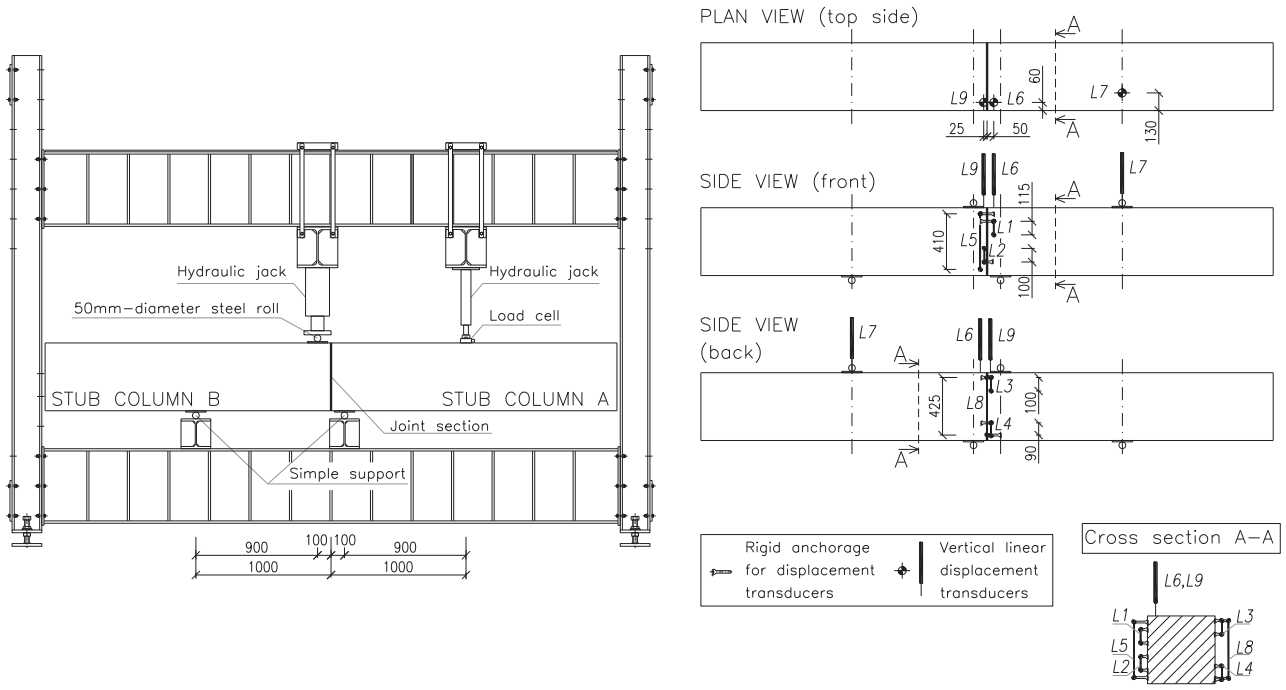

a b

Fig. 23. Shear test: (a) test setup (side view) and (b) locations of the linear displacement transducers. Dimensions in mm.

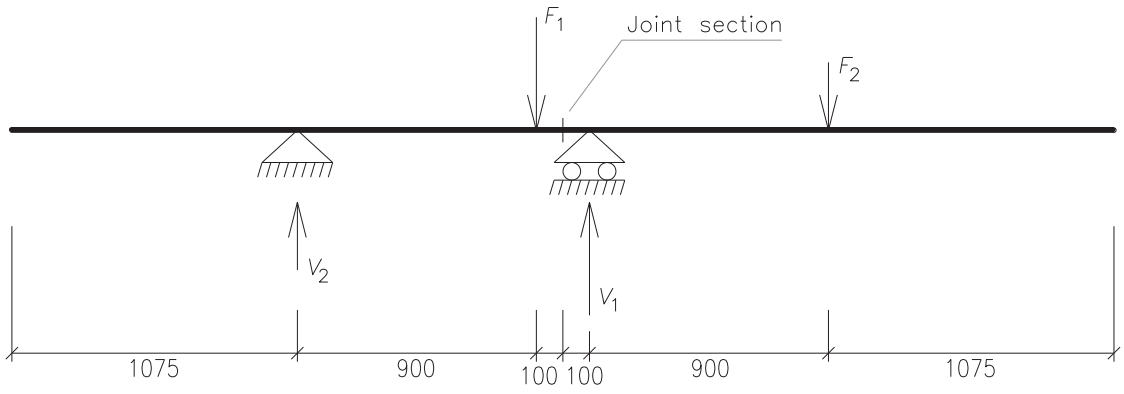

$V_1 = (9/11)F_1 + (20/11)F_2$

$V_2 = (2/11)F_1 - (9/11)F_2$

Fig. 24. Statically determinate configuration adopted for the shear test. Dimensions in mm.

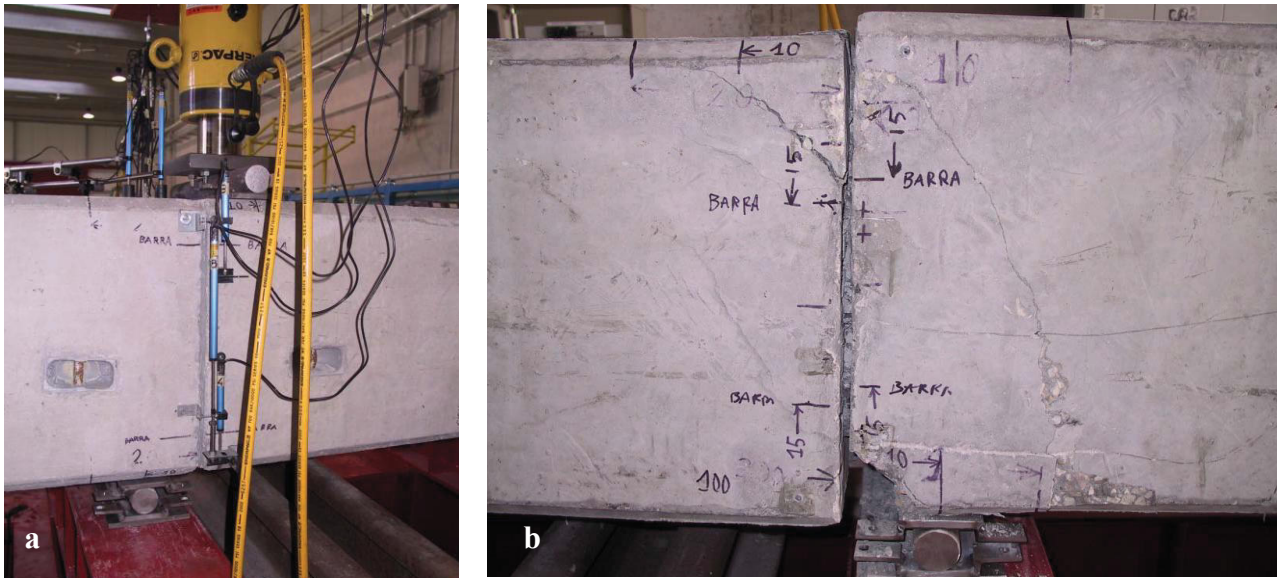

Fig. 25. Shear test: detail views of (a) test setup and (b) joint section at the end of test.

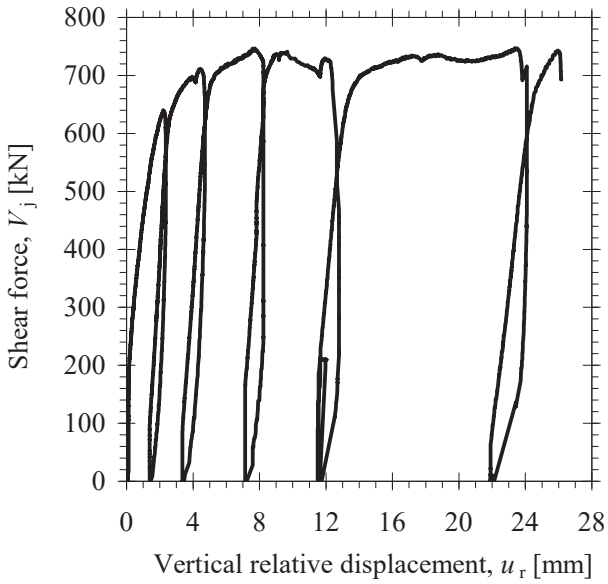

Fig. 26. Shear test: plot of the shear force versus vertical relative displacement at the joint section.

Table 1. Concrete and grout compressive strengths obtained from tests on cubic specimens.

Test	Concrete age, t [days]	$\beta_{cc}(t)$	$f_{cm,cube}(t)$ [MPa]	$f_{cm,cube}(28)$ [MPa]
Direct tensile test	43	1.039	69.7	67.0
Four-point bending test	51	1.053	68.7	65.2
Cyclic bending test	187	1.130	72.0	63.7
Test with combined bending and axial load	62	1.068	69.7	65.3
Shear test	62	1.068	71.2	66.6
Grout 1	29	1.003	74.8	74.5
Grout 2	56	1.060	82.9	78.2

Table 2. Mean values of the mechanical properties for reinforcing steel.

Bar diameter [mm]	E_{sm} [GPa]	f_{ym} [MPa]	f_{tm} [MPa]	f_{tm}/f_{ym}	ε_{um} [%]
8	Not available	457	493	1.08	18
20	198	517	633	1.22	23

Table 3. Points of the envelope diagrams obtained from the cyclic bending test: values of jack half-load (P), deflection under the load (u_l), drift (θ) and curvature (χ).

P [kN]	u_l [mm]	θ [%]	χ [1/m]	P [kN]	u_l [mm]	θ [%]	χ [1/m]
62.5	3.1	0.19	0.01	–63.1	–2.9	–0.18	–0.02
125.6	8.1	0.51	0.04	–125.0	–8.0	–0.50	–0.03
144.0	11.1	0.69	0.05	–143.8	–11.4	–0.71	–0.06
155.0	14.8	0.93	0.09	–154.4	–13.9	–0.87	–0.09
167.5	24.8	1.55	0.23	–165.0	–25.3	–1.58	–0.24
160.0	35.0	2.19	0.37	–150.0	–33.4	–2.09	–0.39
129.4	36.8	2.30	0.38	–139.4	–33.4	–2.09	–0.39
133.1	46.3	2.89	0.53	–145.0	–55.5	–3.47	–0.68
137.5	61.5	3.84	0.72				

Table A.1. Parameters used in Tables A.2 and A.3.

Symbol, description [Units]		Equation	Value
$H=B$	Cross-section dimensions [mm]		500
$\varnothing_b$	Diameter of longitudinal reinforcing bars [mm]		20
$\varnothing_{dp}$	Drainpipe diameter [mm]		100
A_{si}	Area of the i-th reinforcement layer [mm^2]		
	Cross-section D-D in Fig. 1c (i = 1, ..., 3)	$A_{s1}=A_{s3}=3\pi\varnothing_b^2/4$; $A_{s2}=2\pi\varnothing_b^2/4$	942; 628
	Cross-section B-B in Fig. 1c (i = 1, ..., 4)	$A_{si} = 2\pi\varnothing_b^2/4$ (i = 1, ..., 4)	628
d_i	Distance of A_{si} from the top [mm]		
	Cross-section D-D in Fig. 1c (i = 1, ..., 3)		60; 250; 440
	Cross-section B-B in Fig. 1c (i = 1, ..., 4)		80; 150; 350; 420
d	Effective depth [mm]		
	Cross-section D-D in Fig. 1c		440
	Cross-section B-B in Fig. 1c		420
I_s	Second moment of area of bars [m$^4\times10^5$]		
	Cross-section D-D in Fig. 1c	$I_s = \sum_i A_{si}(d_i - H/2)^2$	6.805
	Cross-section B-B in Fig. 1c		4.888
A_s	Total reinforcement area (cross-sections B-B and C-C in Fig. 1c) [mm^2]	$A_s = 8\pi\varnothing_b^2/4$	2512
A_{slap}	Total reinforcement area in the lap zone (cross-sections A-A and C-C in Fig. 1c) [mm^2]	$A_{slap} = 2A_s$	5024
E_s	Young's modulus of reinforcing steel [GPa]		200

Table A.2. Specimen subjected to axial tension. Evaluation of the slopes of N-ε linear responses for uncracked concrete (UC) and reinforcing bars (see Fig. 7).

Symbol, description [Units]		Equation	Value
E_{ci}	Initial modulus of concrete [GPa]	$E_{ci} = 5.7(f_{cm,cube})^{0.5}$	47.6
n_i	Ratio of steel to concrete moduli	$n_i = E_s/E_{ci}$	4.20
Joint section (cross-section B-B in Fig. 1c)			
E_sA_s	Axial rigidity of bars [kN×10^{-5}]		5.025
E_sI_s	Bending rigidity of bars [kNm^2×10^{-3}]		9.772
Lap zone (cross-sections A-A and C-C in Fig. 1c)			
A_I	Homogenized concrete section [m^2×10^1]	$A_I = H^2 - \pi\varnothing_{dp}^2/4 + n_iA_{slap}$	2.633
K_I	Slope of N-ε response, UC [kN×10^{-7}]	$K_I = E_{ci}A_I$	**1.253**
K_{II}	Slope of N-ε response, bars [kN×10^{-6}]	$K_{II} = E_sA_{slap}$	**1.005**

Table A.3. Specimens subjected to monotonic bending (MB), cyclic bending (CB) and combined axial compression and bending (AB). Evaluation of the slopes of P-u_m, P-u_l and M-χ linear responses for uncracked (UC) and cracked concrete (CC).

Symbol, description [Units]		Equation	Value		
			Test MB	CB	AB
L	Span length [m]		4.0	4.0	3.4
a	Load-to-support distance [m]		1.4	1.6	1.4
N	Maximum axial load [kN]		0	0	1741
N_0	Initial axial load [kN]		0	0	1620
E_{ci}	Initial modulus of concrete [GPa]	$E_{ci} = 5.7(f_{cm,cube})^{0.5}$	47.2	48.4	47.6
n_i	Ratio of steel to concrete moduli	$n_i = E_s/E_{ci}$	4.23	4.14	4.20
E_{cm}	Secant modulus of concrete [GPa]	$E_{cm} = 22(f_{cm}/10)^{0.3}$	37.1	37.6	37.2
n_m	Ratio of steel to concrete moduli	$n_m = E_s/E_{cm}$	5.39	5.32	5.37
UC Sections					
A_I	Homogenized concrete section [$m^2 \times 10^1$]	$A_I = H^2 - \pi \varnothing_{dp}^2/4 + n_i A_{si}$	2.528	2.525	2.527
I_I	Second moment of area [$m^4 \times 10^3$]				
	Cross-section D-D in Fig. 1c	$I_I = H^4/12 + n_i I_s - \pi \varnothing_{dp}^4/64$	5.491	5.485	5.489
	Cross-section B-B in Fig. 1c		5.410	5.406	5.409
M_{cra}	Cracking moment[a] [kNm]				
	Cross-section D-D in Fig. 1c	$M_{cra} = I_I/(H/2)(N_0/A_I + f_{ctm})$	87.9	87.8	87.0
	Cross-section B-B in Fig. 1c		86.6	86.5	86.5
K_I	Slope of P-u_m response[b] [$kN/m \times 10^{-5}$]	$K_I = 8E_{ci}I_I/\{(aL^2)[1-(4/3)(a/L)^2]\}$	**1.107**[e]	1.054	1.668
	Slope of P-u_l response[b] [$kN/m \times 10^{-5}$]	$K_I = 2E_{ci}I_I/\{(a^2L)[1-4a/(3L)]\}$	1.241	**1.110**[g]	**1.738**[h]
	Slope of M-χ response[c] [$kNm^2 \times 10^{-5}$]	$K_I = E_{ci}I_I$	**2.556**[f]	2.614	**2.574**[i]
CC Sections					
y_n	Neutral axis depth[d] [mm]	Solution to:			
	Cross-section D-D in Fig. 1c	$By^2/2 - n_m \sum_i A_{si}(d_i - y) = n_m(d-y)N/f_y$	92.4	91.9	158.9
	Cross-section B-B in Fig. 1c		92.4	91.9	155.6
I_{II}	Second moment of area [$m^4 \times 10^4$]				
	Cross-section D-D in Fig. 1c	$I_{II} = By_n^3/3 + n_m \sum_i A_{si}(d_i - y_n)^2$	8.351	8.252	11.460
	Cross-section B-B in Fig. 1c		7.317	7.233	10.107
M_{0a}	Intercept of M-χ response[j] [kNm]				
	Cross-section D-D in Fig. 1c	$M_{0a} = N(H/2 - y_n)$	0.0	0.0	164.4
	Cross-section B-B in Fig. 1c		0.0	0.0	158.6
M_{ya}	Yielding moment [kNm]				
	Cross-section D-D in Fig. 1c	$M_{ya} = M_{0a} + f_y I_{II}/[n_m(d - y_n)]$	230.4	230.5	551.2
	Cross-section B-B in Fig. 1c		214.2	214.4	532.5
K_{II}	Slope of P-u_m response[b] [$kN/m \times 10^{-4}$]	$K_{II} = 8E_{cm}I_{II}/\{(aL^2)[1-(4/3)(a/L)^2]\}$	**1.322**[e]	1.233	2.727
	Slope of P-u_l response[b] [$kN/m \times 10^{-4}$]	$K_{II} = 2E_{cm}I_{II}/\{(a^2L)[1-4a/(3L)]\}$	1.481	**1.299**[g]	**2.841**[h]
	Slope of M-χ response[c] [$kNm^2 \times 10^{-4}$]	$K_{II} = E_{cm}I_{II}$	**2.714**[f]	2.721	**3.765**[i]

[a] Evaluated for mean concrete tensile strength $f_{ctm} = 4$ MPa estimated in accordance with [30];
[b] Referred to cross-section D-D in Fig. 1c;
[c] Referred to cross-section B-B in Fig. 1c;
[d] Computed for $f_y = 517$ MPa (see Table 2) for test AB; f_y is ineffective for tests MB and CB;
[e–i] Bold values are the slopes of the dashed lines in: [e] Fig. 10; [f] Fig. 11; [g] Fig. 17; [h] Fig. 21a and [i] Fig. 21b
[j] Intercept of M-χ response for CC reported in Fig. 21b